Title
Renewable Polymeric Energy Harvesters from Moisture and Heat

Author
Long, Yu

Publication Date
2022

Peer reviewed|Thesis/dissertation

Renewable Polymeric Energy Harvesters from Moisture and Heat

By

Yu Long

A dissertation submitted in partial satisfaction of the

requirements for the degree of

Doctor of Philosophy

in

Mechanical Engineering

in the

Graduate Division

of the

University of California, Berkeley

Committee in charge:

Professor Liwei Lin, Chair
Professor Grace Gu
Professor Dorian Liepmann

Spring 2022

Abstract

Renewable Polymeric Energy Harvesters from Moisture and Heat

by

Yu Long

Doctor of Philosophy in Mechanical Engineering

University of California, Berkeley

Professor Liwei Lin, Chair

Electricity is indispensable in our daily life and batteries are the widely used energy sources for portable devices in the modern world. However, harmful chemicals and wastes in batteries can lead to serious environmental and health problems without proper dispositions. As such, renewable energy sources such as solar cells have drawn lots of interests with great progresses in recent years. In this work, two forms of renewable energy harvesters based on polymers are studied based on moistures and thermal gradients in the environment. Material properties, fundamental operation mechanisms, and application demonstrations of these two renewable energy harvesters are investigated in the dissertation.

The moisture-based electric generators have long working time and high energy density output by utilizing the mechanism of the proton transportation and proton concentration oscillation. The specific polymer used in the generator has a moisture-induced oscillation surface potential from the functional groups of the polymer. Both dynamic simulation and oscillation theory have been developed to analyze this phenomenon. The self-oscillation behavior help extending the operation period of the energy harvester under the constant feeding of moistures. Experimental results show the short-circuit current density can reach 1.5 $\mu A/cm^2$ and a maximum open-circuit voltage of 0.4 V with a long operation period up to 15,000 seconds with an energy density of 16.8 mJ/cm^2.

The thermoelectric energy harvester has an ultra-high Seebeck coefficient and self-healing properties, which is suitable for harvesting energy from temperature gradients such as wearable devices between the human skin and the environment. The energy generator is based on the material of ionogel, which has different pore sizes and polarities to results in the very different diffusion coefficients of anions and cations. Specifically, the diffusion coefficients are characterized and simulated by using the molecular dynamic simulation under different temperatures and tested experimentally. The whole device has a measured Seebeck coefficient at 298 μV/K, which is generally higher than those of traditional thermoelectric materials. Furthermore, the prototype device is flexible, bendable and self-healable for potential applications in harvesting electrical energy for wearable devices.

Table of contents

List of figures

List of tables

Acknowledgments

Throughout the writing of this dissertation, I have received a great deal of support and assistance, to which I would like to express my acknowledgments here.

I would first like to thank my supervisor, Professor Liwei Lin, whose expertise was precious in formulating the research questions and methodology. His insightful feedback helped me to sharpen my thinking and brought my work to a higher level.

I would also like to acknowledge my lab mates in LinLab, especially Mr. Peisheng He, Mr. Yande Peng and Dr. Junwen Zhong who is now a professor in the University of Macau. Our discussions and their kind help during my research inspired me a lot.

In addition, I would like to thank my boyfriend, Mr. Banghua Zhu, and my little cat, Oreo. They gave me invaluable emotional support to enrich my student life experiences at Berkeley. A special thank is given to my dear grandfather, Mr. Chunbao Pei, although he was unable to see this and share my happiness anymore. I could not be what I am today without him. You are always by my side, my dear grandpa.

1. Introduction

1.1 Battery wastes and green energy

Electricity has become indispensable in our daily life and many modern devices have been powered by electricity generated from large power plants, while batteries have been the key energy sources for portable devices [1]. However, improper disposition of batteries can cause serious environmental problems – when they are throwed away into trash, they end up in landfills. They contain hazardous, toxic, and corrosive materials like mercury, cadmium, lithium, and lead. After they decay and leak, the corrosive liquids and dissolved metals will be released into air and water and soaked into soil to contaminate groundwater and surface water. Eventually, they can turn into human bodies [2].

Besides promoting the recycling processes, renewable energy, which is derived from natural processes and able to replenish constantly, can be a good substitute for batteries. In the past decades, green energy have emerged as alternative power resources, such as solar cells which convert sun light to electricity [3], [4], and piezoelectric or triboelectric energy generators which convert ambient vibration to electrical energy [5]. In this dissertation, two green energy harvesters based on polymers are introduced and discussed. The first is a moisture-based electric generator, which harvests energy in a high humidity environment. The second is a thermoelectric generator, which harvests energy from the temperature gradient. The materials, device structures, fundamentals and performances are discussed and illustrated in later sections.

1.2 Moisture electric generator

Recently, a new class of energy harvester has been demonstrated by the moisture-electric effect based on the mechanisms of proton transportations [6]–[15], ion transportations [16]–[18], and electrokinetic reactions [19]–[22]. Usually, the devices based on electrokinetic reactions can work for a very long time under a constant moisture feeding process, while their current density output is quite low (typically in the nA/cm^2 level). On the contrary, devices based on proton/ion transportation mechanisms have larger energy density outputs. However, the outside humidity needs to be changed to activate the energy generation process. This is because the active ion concentration (for example, proton concentration) reaches equilibrium at the two electrode sides during the energy generation process and the outside humidity level has to be changed to initiate another energy generation process [12]. In these systems, the operation time period is intermittent as it is induced by the moisture stimulation in one hydration/dehydration cycle [22].

Since the humidity level does not quickly increase and decrease for the hydration/dehydration cycle in the ambient environment, most reported moisture-electric devices have limited energy outputs. One approach to increase the output energy is to use “protein nanowires”[23] for the continuous electric power generation in the ambient environment. This approach can limit the immigration of free protons in the materials to increase the working period.

A very different approach is illustrated in this dissertation work based on the phenomenon of “self-excited proton concentration oscillations” by a carefully designed material system to drastically

improve the operation period and electrical energy outputs for the moist-electric generator. Due to the proton concentration oscillations, the proton concentration at two electrode sides will not be at the equilibrium state for a very long time. Therefore, the operation period has a significant improvement as compared with the other generators based on the proton transportation mechanism without sacrificing the energy density outputs.

1.3 Thermoelectric generator

Statistical data have shown that more than 60% of the energy generated worldwide is lost in the form of wasted heat [24] such that harvesting energy from various heat sources could make drastic impact to the global energy issues. A thermoelectric energy harvester is a promising solution to sustainably produce energy directly from heat sources. They have distinctive advantages in: (1) having the possibility to harvest energy from both hot or cold surfaces, and (2) being eco-friendly to produce energy without using fossil fuel to result in the reduction in greenhouse gas emissions. It is well-known that a heat source can be converted to electric power utilizing the thermoelectric effect due to the movements of charge carriers under a thermal gradient. The ratio between the generated voltage ΔV and the temperature gradient ΔT is defined as the Seebeck coefficient:

$$S = \frac{\Delta V}{\Delta T} \qquad (1)$$

A high Seebeck coefficient is favorable for the energy conversion performances toward practical applications in systems such as portable electronics and wearable devices [25]–[27]. A figure of merit value, *zT,* at temperature, T, has commonly used to evaluate the performance as:

$$zT = \frac{\sigma S^2 T}{\kappa} \qquad (2)$$

where σ is the electrical conductivity and κ is the thermal conductivity of the material. These two properties are often coupled with each other by means of the transportations of electrons and holes such that it has been challenging to increase the figure of merit value for most materials. However, the electric carriers can be ions, and the heat carriers can be phonons. Hence, ionogel systems can be constructed in which the transportations of electricity and heat are separated.

1.4 Dissertation contributions

This dissertation research focuses on the two works related to renewable energy harvesters. One is a moisture electric generator, and the other is a thermoelectric harvester. In both parts, the materials, their fabrications and characterizations are introduced in detail. The fundamentals and mechanisms are also illustrated and supported by simulations. The performances of prototype devices are discussed and compared with other reported works.

Chapter 2 introduces the moisture electric generator based on the polymer material - poly([2-(methacryloyloxy)ethyl] dimethyl-(3-sulfopropyl) ammonium hydroxide-co-acrylic acid), which has a unique phenomenon in moisture-induced electrical potential oscillations (**Fig. 1a**). To understand the basics, chemical reactions are modeled by kinetic simulations and the stability matrix is analyzed to show the chaotic nature of the system which oscillates with hidden attractors to induce the autonomous surface potential oscillation. Using moisture in the ambient environment as the activation source, this

self-excited chemoelectrical reaction could have broad influences and usages in surface-reaction based devices and systems. As a proof-of- concept demonstration, an energy harvester is constructed and its performances are measured (**Fig. 1b**). A liquid crystal display is powered with five energy harvesters connected in series toward practical applications.

Chapter 3 introduces the thermoelectric generator. The generator is based on an ionogel, in which both the anions and cations move under temperature gradients (**Fig. 1c**). Due to the difference in sizes and polarities, their diffusion coefficients have large differences. The molecular dynamic simulation has been utilized to verify this phenomenon (**Fig. 1d**). Experimental results show the prototype devices have very high Seebeck coefficients as compared with those of traditional metal or ceramic based thermoelectric harvesters. Together with flexible and self-healable properties, these energy harvesters could be suitable for the applications in flexible and wearable electronics.

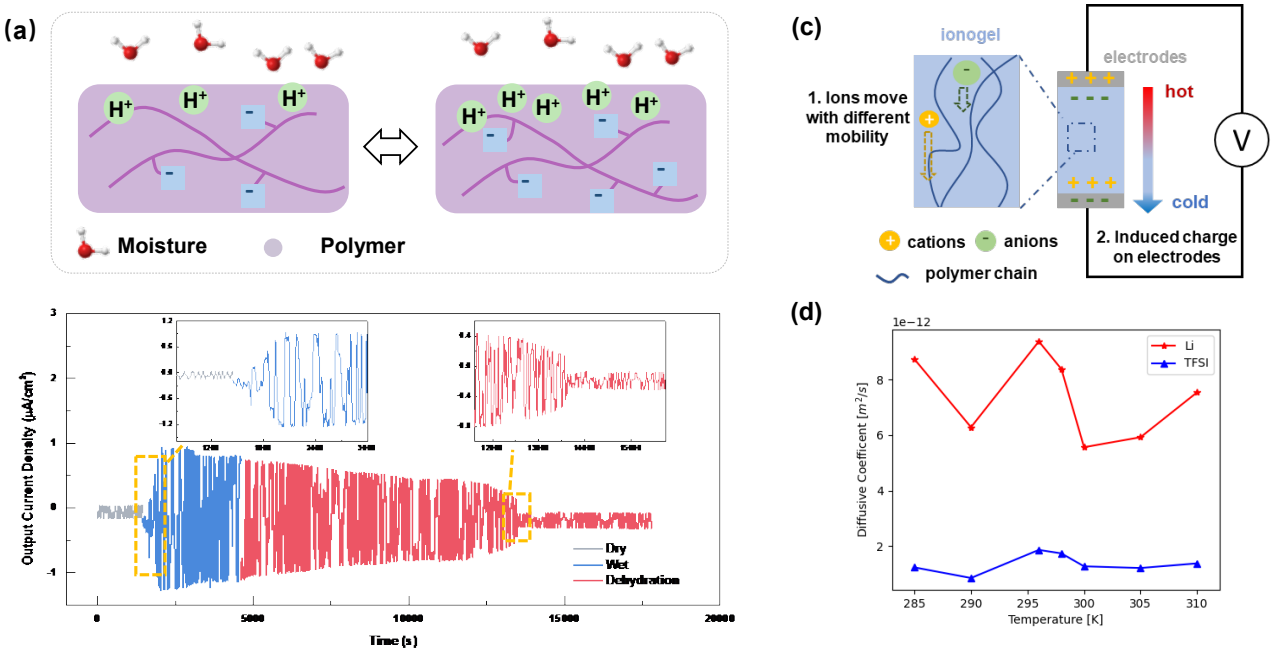

Fig. 1. (a) Illustration of the self-oscillation of the polymer under moisture. **(b)** A real-time current signal output of the moisture electric generator. **(c)** Schematic of the ionogel-based thermoelectric generator. **(d)** The simulation results of the diffusion coefficients of anions and cations.

2. Moisture-induced autonomous surface potential oscillations for energy harvesting

2.1 Surface potential oscillation

In practice, forced oscillation is a phenomenon to induce repetitive variations by changing the external stimulations, such as force, temperature, light, or electricity input, *etc*.[28]–[32] On the other hand, autonomous oscillations or "self-oscillating" behaviors are the alternating activities without repetitive external stimulations.[33]–[37] Autonomous oscillations exist widely in living organisms, such as heartbeats, brain waves, and some biochemical reactions[35]. Mimicking and applying these autonomous oscillations in artificial systems have attracted great interests for practical applications. For example, prior efforts have utilized the periodically swelling and de-swelling behavior of polymeric materials caused by the moisture diffusion process induced by sunlight as actuators.[38] Other polymer-based autonomous oscillations have also been demonstrated for applications in artificial muscles, drug delivery systems, and biosensors, … *etc*.[38]–[42]

Here, autonomous electrical potential oscillations induced by the moisture diffusion process in P(MEDSAH-co-AA) are studied. It is found that the surface electrical potential of this polymer system can oscillate continuously upon the exposure to moisture to result in the generation of close-circuit alternating current (AC) outputs – this is very different from the previously reported mechanism of direct current (DC) outputs by moisture effects.[15] Experimentally, a porotype energy harvester has been constructed to utilize the autonomous oscillation mechanism with a maximum open-circuit voltage and short-circuit current density of 0.4 V and 1.5 μA/cm^2, respectively. Furthermore, this device is reusable and the operation time period under one moisture excitation can achieve 15,000 seconds, with an energy density of 16.8 mJ/cm^2. The voltage output can be further increased to 2 Volts by connecting five energy harvesters in series to light up an LCD in a bathroom.

2.2 Materials and basic mechanism

One common oscillation example in nature is the concentration of Calcium in living cells to assist the transmission of intracellular biological information.[43], [44] The Calcium-induced Ca^{2+} release (CICR) process is illustrated in **Fig. S1**, where the inositol trisphosphate (IP_3) helps the releasing of Ca^{2+} into the cytoplasm from the 1st pool, leading to an increase in Ca^{2+} concentration as a positive feedback process. Some similar comparisons can be made for the observed moisture-induced surface potential oscillation phenomenon as the H^+ concentration can oscillate with the help of moisture. In the CICR process, some released Ca^{2+} ions are pumped back to the 1st pool and a 2nd pool of Ca^{2+} also exists in the cytoplasm to release or absorb Ca^{2+} in response to the concentration of the free Ca^{2+}. As a result, the Ca^{2+} concentration oscillates continuously. The surface potential of the polymeric material, P(MEDSAH-co-AA) polymer as shown in **Fig. 2a**, also oscillates as observed in this work. The polymer is synthesized by a free-radical polymerization method[45] with two monomers, [2-(methacryloyloxy)ethyl] dimethyl-(3-sulfopropyl) ammonium hydroxide (MEDSAH) and acrylic acid

(AA), initiated by the ammonium persulfate (APS) and polymerized with detailed process as shown in **Fig. S2**. The ratios of MEDSAH and AA monomers (MEDSAH/AA) in the prototypes are 1/2, 1/3, and 1/4, respectively. To characterize monomer distributions inside the polymer, the energy-dispersive X-ray (EDX) spectroscopy is performed and the N-Kα line is chosen to represent MEDSAH. **Figure S3** to illustrate that the two monomers are homogeneously distributed in the prototypes of varying MEDSAH/AA ratios. The synthesized polymer is transparent (inset picture in **Fig. 2a**) and it contains the N^+, $-SO_3^-$, and -COOH groups which play key roles in the surface potential oscillation process.

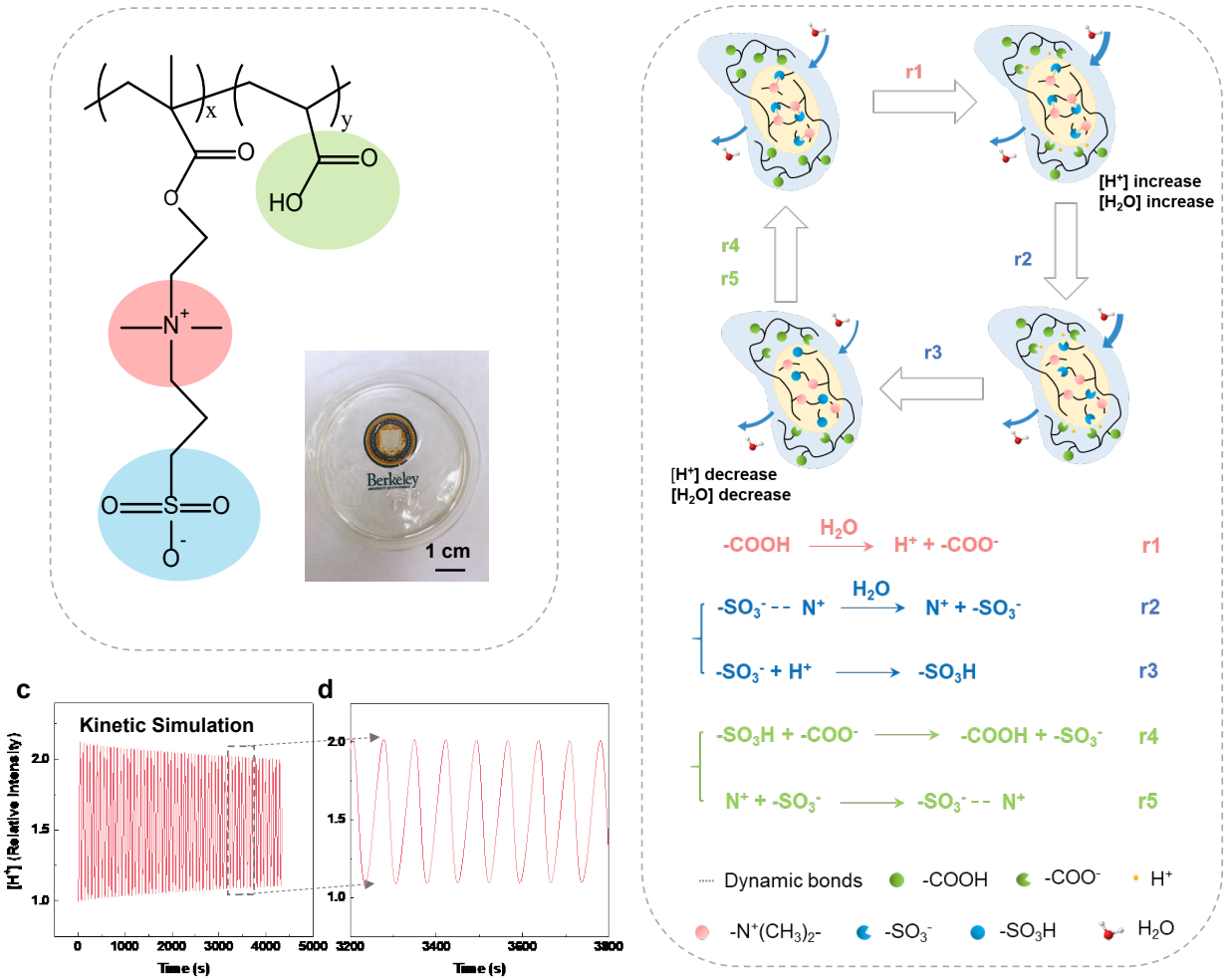

Fig. 2. Materials and mechanism of proton oscillation system. **(a)** The chemical structure of the as-synthesized P(MEDSAH-co-AA) polymer with key chemical groups which produce the autonomous oscillation of the surface potential. Inset: an optical photo showing the synthesized and transparent polymer film. **(b)** Schematic illustrations of the proton transportation process via the functional groups of N^+, $-SO_3^-$, and -COOH in P(MEDSAH-co-AA) with related chemical reactions: (r1) the proton generation in the positive feedback process, (r2, r3) the proton reduction in the negative feedback processes, and (r4, r5) intermediate interactions. **(c)** Kinetic simulation results of the H^+ concentration

versus time from the chemical reactions. **(d)** Enlarged view of the kinetic simulation result in (c).

A detailed model is developed to qualitatively explain the electrochemical oscillation process by the related chemical reactions from r1 to r5 in **Fig. 2b**. The model starts with the release of protons upon the introduction of moisture to activate the functional groups in the polymer as evidenced from the Attenuated Total Reflectance Fourier-transform infrared (ATR-FT-IR) spectroscopy (**Fig. S4**). Specifically, the carboxylic acid (-COOH) groups can generate free protons upon the exposure to moisture (r1), which increases the polarity and attracts moistures to accelerate the ionization process. This moisture attraction behavior is further validated in **Fig. S5**, where polymers with high -COOH contents can absorb moisture at a faster speed in the hydration process and maintain higher moisture concentrations during the dehydration process as compared with those of polymers with low -COOH contents**.** As a result, the free proton concentration increases as the positive feedback process. Moistures also helps breaking the dynamic bonds between N^+ and $-SO_3^-$ groups (r2), and the SO_3^- groups can capture protons (r3) to form the sulfonic acid ($-SO_3H$). These two reactions are responsible for the reduction of the proton concentration as the negative feedback processes. Furthermore, protons are transported from the sulfonic acid to the carboxylic acid and -COOH (r4) and the dynamic bonds between the N^+ and $-SO_3^-$ groups will re-formulate (r5). The overall processes from r1 to r5 (**Fig. S6**) show that N^+, $-SO_3^-$, and -COOH groups complete their individual cycles as moistures diffuse into the P(MEDSAH-co-AA) polymer to assist the self-sustained proton concentration oscillation phenomenon, which results in the surface electrical potential oscillation. Based on these chemical reactions, a kinetic model is established to qualitatively explain the autonomous oscillation mechanism and the exemplified simulation results are shown in **Figs. 2c and 2d**. It is found that the proton concentration may oscillate while the relative intensity of the proton concentration decreases gradually over time. The reduction of the proton concentration magnitude over time is also found in the Calcium oscillation process in the living cells.[44] Specifically, simulation results show that the surface proton intensity decreases to around 87% of its original value after 2,000 seconds and oscillate at about 70 seconds per cycle for a prototype device by adjusting the parameters to match the experimental observations. By changing the kinetic parameters in the simulation, the oscillation period and intensity degradation will change and these parameters are studied with details in **Supporting Explanation 1**.

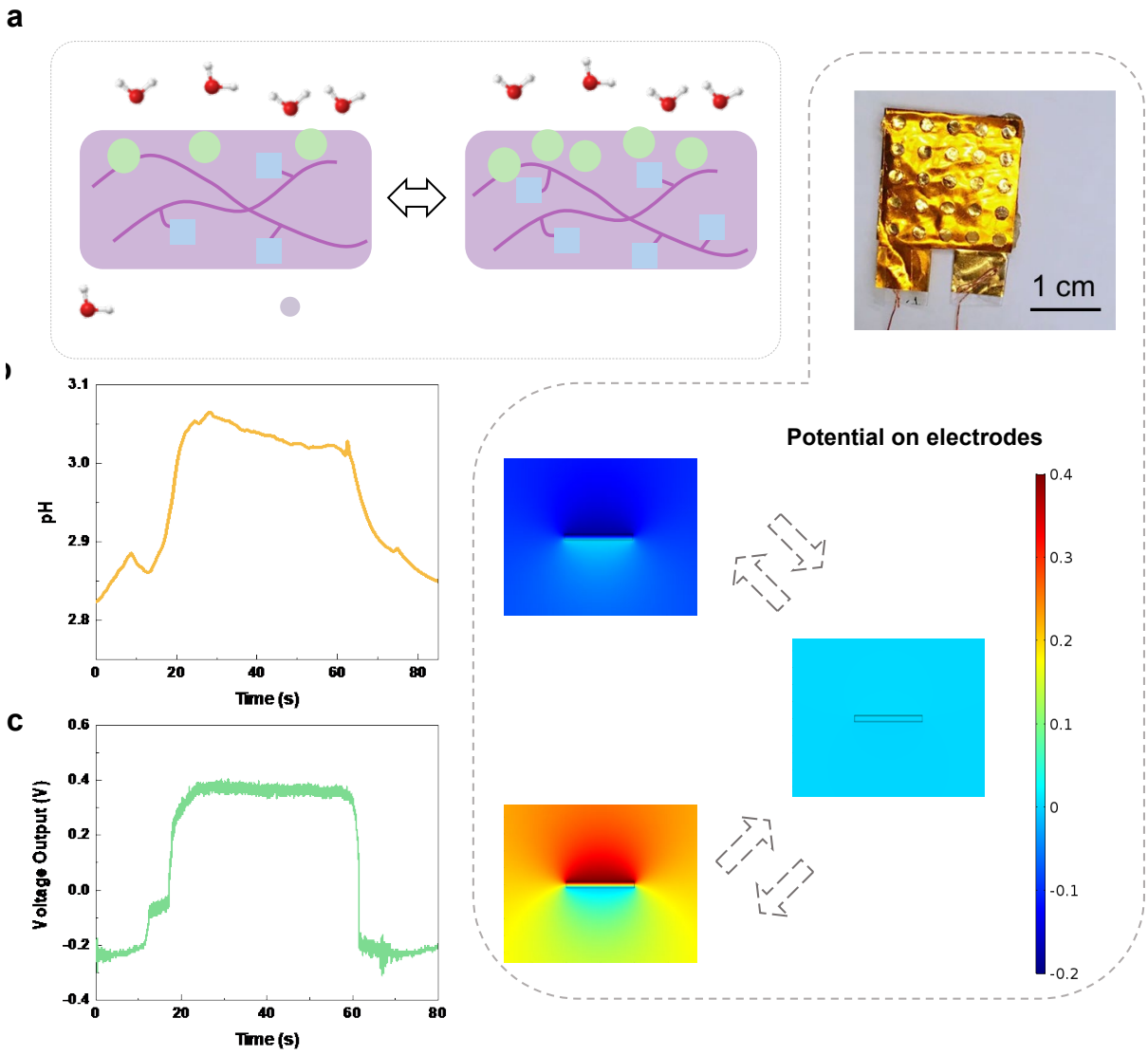

Fig. 3. (a) A schematic diagram showing the surface potential oscillations of P(MEDSAH-co-AA). **(b)** The measured pH vs. time plot for the P(MEDSAH-co-AA) polymer surface in one cycle. **(c)** Measured voltage vs. time curve in one cycle. **(d)** An optical photo of a fabricated energy harvester based on P(MEDSAH-co-AA) polymer and COMSOL simulation results showing the surface potential oscillation of an energy harvester versus time.

Figure 3a illustrates the surface potential oscillation on the synthesized polymer due to the proton (H^+) concentration oscillation. Experimentally, the surface proton concentration oscillation is characterized by using a pH sensor. **Figure 3b** shows the measured pH vs. time plot in one cycle and **Figure 3c** shows the measured voltage vs. time plot of the energy harvester in one cycle. These real-time measurement results demonstrate the proton/voltage oscillation phenomenon. This behavior is believed to come from the chemical potential change as the moisture from the environment diffuses

through the polymer structure. Specifically, the chemical potential of water moisture in a high humidity environment is higher than that of absorbed moisture in the polymer. As a result, the change of Gibbs free energy in the absorbed moisture is converted to electric energy in the chemical potential-based energy harvester.[6] In another test, the KPFM analysis is used to show the surface potential oscillations in a longer, 12-minute time period (**Fig. S7**).

The self-excited oscillation is further analyzed in **Supporting Explanation 2** by establishing basic equations based on chemical reactions of r1 to r5 and the conservation of matters. Afterwards, small perturbations are added to each variable and the system dynamic equations are derived. The stability matrix and phase portraits of the dynamic equations are then analyzed and it is found that the system has the chaotic nature and oscillates with hidden attractors.[42] As a result, this moisture-induced autonomous surface potential oscillation phenomenon is characterized as a chaotic system with no equilibria in favor of extending the operation period. Another resemblance is utilized based on the biological Calcium-induced Ca^{2+} release (CICR) process in **Supporting Explanation 3**. Specifically, the IP_3 in the CICR process plays a role similar to H_2O to start the proton concentration oscillation process. The 1st pool in the CICR process is in analogy to the -COOH group for the positive feedback process, and the 2nd pool in the CICR process is in analogy to and -SO_3^- group for the negative feedback process to result in the Ca^{2+}oscillation process in living cells.

The moisture-induced surface potential oscillation is applicable for the energy harvesting applications. Previously, several reports have shown moisture-enabled energy harvesters with DC (direct current) outputs[43–46]. This work demonstrates moisture-induced AC power outputs under a relatively constant moisture level. **Figure 3d** shows the top view optical photo of a prototype energy harvester made of MEDSAH/AA with a ratio of 1/2 and 2×2 cm^2 in size. The device has one synthesized P(MEDSAH-co-AA) layer sandwiched by two electrodes made Au coated on a Polyimide (PI) film and the cross-sectional view is shown in **Fig. S8**. The top electrode has circular holes of 2 mm in diameter to allow the direct exposure to moistures. If the P(MEDSAH-co-AA) layer is replaced with a typical copy paper, no visible electrical outputs can be identified (**Fig. S9**) and this result eliminates the possible influence of the electrochemical reactions at the junctions of gold electrodes and copper wires. The surface potential oscillations on the polymer film can induce the electrostatic potential oscillations on the top electrode, which results in AC outputs as demonstrated in COMSOL simulation results in **Fig. 3c** and **Movie S1**. The electrostatic stationary simulation is implemented here to illustrate electrostatic potential outputs induced by the oscillation of the surface charges. The simulated output voltage range is between -0.2 to 0.4 V, which is consistent with the experimental results in **Fig. 3c**.

2.3 Moisture-induced energy harvester with AC outputs

Experimentally, a specimen has been dried at 30% RH in the ambient environment for 24 hours (reducing the inherent moisture to boost the outputs of a chemical potential energy harvester[6]) before a wetting process via an ultrasonic humidifier (Pure Enrichment Inc.). Experimental results show electricity generations in the form of AC outputs after the introduction of 100% RH moisture at 1,400 seconds by the humidifier. It is found that the short-circuit current density increases initially to a

maximum value of around 1 μA/cm^2 at 2,000 seconds (upper left inset in **Fig. 4a**). The average oscillation period is about 76.7 seconds, which is used as the fitting parameter for the kinetic simulation at 70 seconds (**Fig. 2d**). The open-circuit voltage versus time result is recorded in **Fig. 4b** with an average voltage oscillation period of 70.3 seconds under room temperature and the short-circuit current versus time result is recorded in **Fig. 4c.** Both tests are independently measured due to their different setups such that minor variations are expected. Due to the chaotic nature of the process (**Supporting Explanation 2**), simulations cannot precisely predict the experimental results. Nevertheless, main experimental results are summarized as: (1) the average current and voltage oscillation periods in experiments are at 76 and 70 seconds, respectively; and (2) statistical data show a high number of the operation period around 70 seconds, while the non-operational period (noises with low level outputs) is about 150 seconds (**Fig. S10**).

It is also observed that the current density of the outputs decreases gradually after reaching the peak value. In this test, the humidifier is turned off at 4,500 seconds and the system experiences a natural dehydration process to result in the decrease of the output current (upper right insert in **Fig. 4a**). At around 13,600 seconds, a sudden current density drop is observed. Qualitatively, the moisture attraction and evaporation process may reach the equilibrium state over time and there will be no moisture concentration gradient inside the device. As such, the surface potential oscillation process may stop and the energy generation process ends. Experimentally, it is found that by increasing the external moisture level, the electrical output level also increases (**Fig. S11**) and by placing a small droplet of water on the device will also generate electricity with outputs close to those of energy harvesters exposed to the 100% RH ambient condition (**Fig. S12**). In the endurance test under the 100% RH moisture, this energy generation process can last for a long period of time from around 500 seconds to 15,000 seconds or about 4 hours as shown in **Fig. S13**.

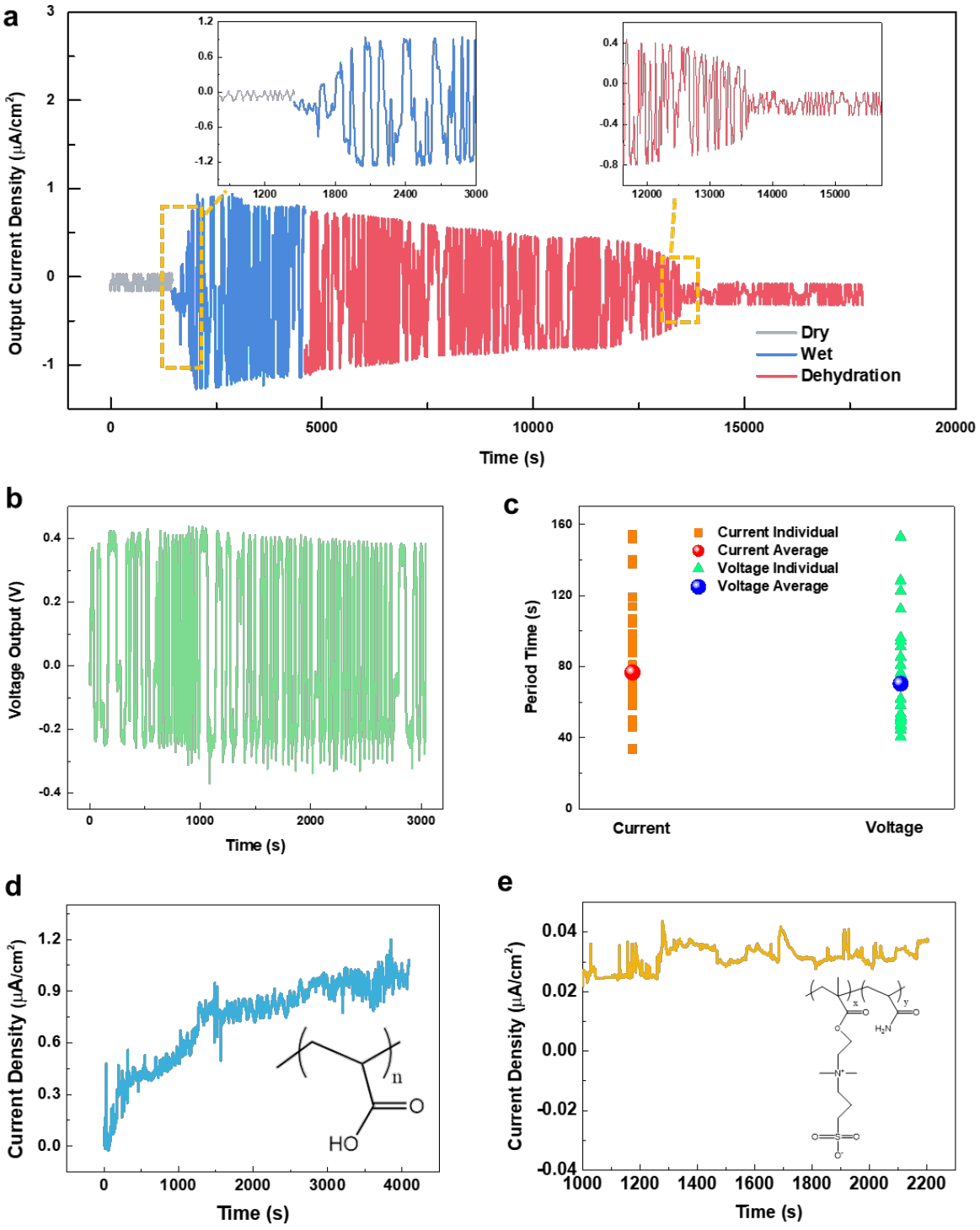

Fig. 4. Performances of a prototype energy harvester based on surface potential oscillations. **(a)** Short-circuit current density versus time of a prototype energy harvester before the introduction of the moisture (grey color), after the moisture wetting process by a humidifier (blue color), and the dehydration process by removing the humidifier (red color). Insets show enlarged views for the wetting (upper left) and dehydration (upper right) processes. **(b)** The open-circuit voltage versus time in the

moisture wetting process by a humidifier. **(c)** The testing results of the working cycle period of the open-circuit voltage and short-circuit current. **(d)** An example of replacing MEDSAH monomer with PAA to remove the SO_3^- and N^+ groups in the polymer, which stops the autonomous oscillations to result in DC electrical outputs. **(e)** In another example, the AA monomer is replaced with acrylamide to remove the -COOH groups and only DC outputs are observed.

Material systems without the key chemical reactions to assist the cyclic process won't be able to induce the self-oscillation process. For example, if the MEDSAH monomer is replaced with poly(acrylic acid) (PAA) to remove -SO_3^- and N^+ groups, testing results show only DC outputs as shown in **Fig. 4d**. In another example, -COOH groups are removed by replacing the AA monomer with acrylamide to result in only DC outputs in **Fig. 4e**. These two counterexamples suggest that the key ingredients and reactions as proposed in the polymer system are indispensable to induce surface potential oscillations for AC outputs of moisture-induced energy harvesters.

2.4 Parameters affecting the outputs and application demonstration

The electrical outputs of moisture-induced energy harvesters have been studied by changing the compositions of P(MEDSAH-co-AA) polymer and the working temperature. Under a background temperature of 28 ºC, the maximum short-circuit current density and open-circuit voltage versus time of energy harvesters with the MEDSAH/AA ratios of 1/2, 1/3, and 1/4 are shown in **Fig. 5a** and the current versus time results are shown in **Fig. S14**. In order to reduce the influence of environmental noises, a capacitor (4.7 μF) has been charged by prototype devices with a rectifier and its voltage outputs have been recorded in **Fig. S15a** and **S15b**. Other energy harvesters with AC outputs such as the piezoelectric and triboelectric energy harvesters also utilize rectifiers to accumulate the AC electricity in the form of capacitors.[47,48] It is found that by increasing the MEDSAH/AA ratios, the maximum current density and voltage increase from 1.2 μA/cm^2 and 0.32 V to 1.7 μA/cm^2 and 0.4 V, respectively, due to the increment of the -COOH groups in the system. The simulation results also predict the increase of oscillation amplitude as the AA composition increases (**Fig. S16**). The average current oscillation period, which is related to the reaction kinetics, is found to maintain at around 72 seconds for all tested polymers of different compositions as depicted in **Fig. 5b**. On the other hand, under a MEDSAH/AA ratio of 1/2, the maximum short-circuit current density and open-circuit voltage of a prototype energy harvester under 12 ºC, 28 ºC, and 60 ºC are tested as shown in **Fig. 5c** (more details in **Fig. S15c** and current outputs in **Fig. S17**). When the temperature is lowered to 12ºC, the maximum current density and voltage slightly decrease to 1.1 μA/cm^2 and 0.30 V, while the average oscillation period increases to 97 seconds (**Fig. S17a**). As the working temperature increases to 60 ºC, the maximum current density and voltage values increase to 1.6 μA/cm^2 and 0.33 V, and the average oscillation period decreases to 57 seconds (**Fig. S17b**). Analytically, the reaction speed is increased at a high temperature environment under energized states and this phenomenon of negative correlation between the temperature and oscillation period is also predicted by simulations in **Fig. S18**.

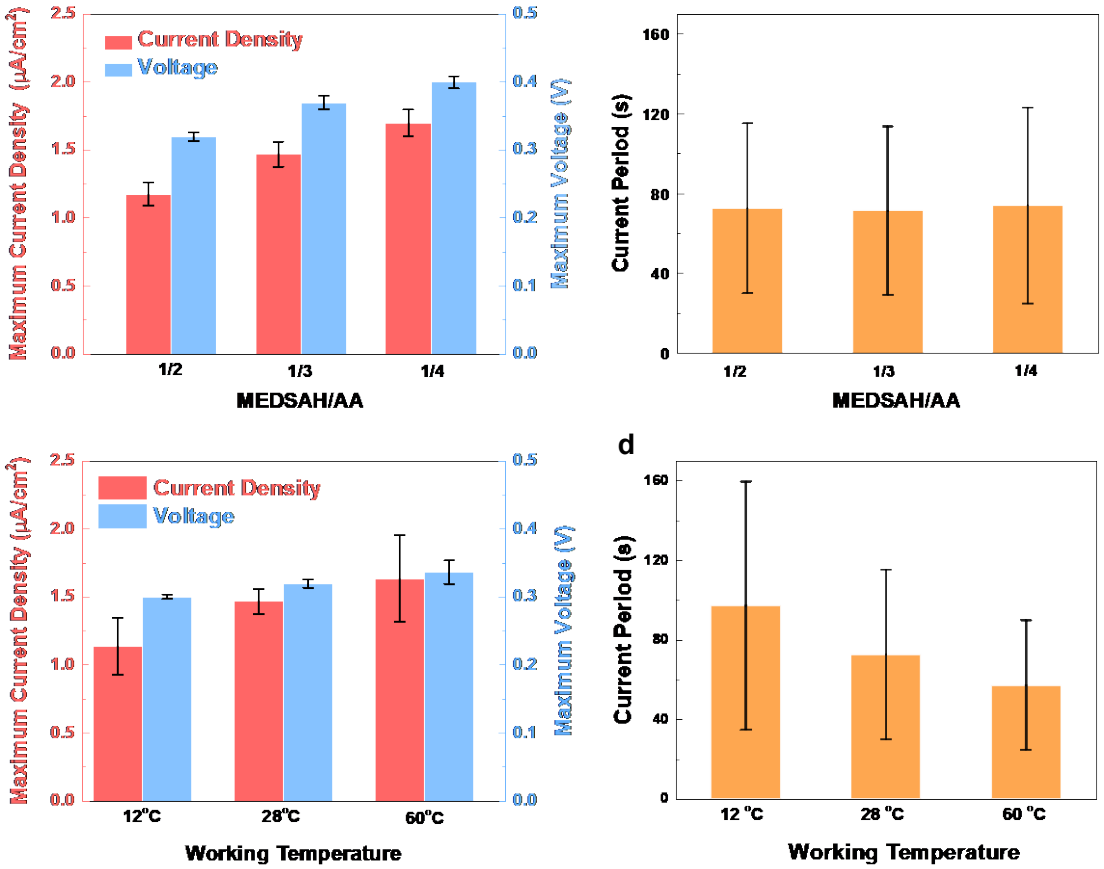

Fig. 5. Electrical output characterizations for moisture-induced energy harvesters with different monomer ratios and under different temperature environments. **(a)** Maximum short-circuit current density and open-circuit voltage for energy harvesters with the MEDSAH/AA ratios of 1/2, 1/3, and 1/4 at 28°C. **(b)** Measured average electrical oscillation output periods of energy harvesters with MEDSAH/AA ratios of 1/2, 1/3, and 1/4, under 28 °C. **(c)** Maximum short-circuit current density and open-circuit voltage of energy harvesters at operating temperatures of 12, 28, and 60°C, respectively. **(d)** Measured average electrical oscillation output periods of energy harvesters at temperatures of 12, 28, and 60 °C, respectively.

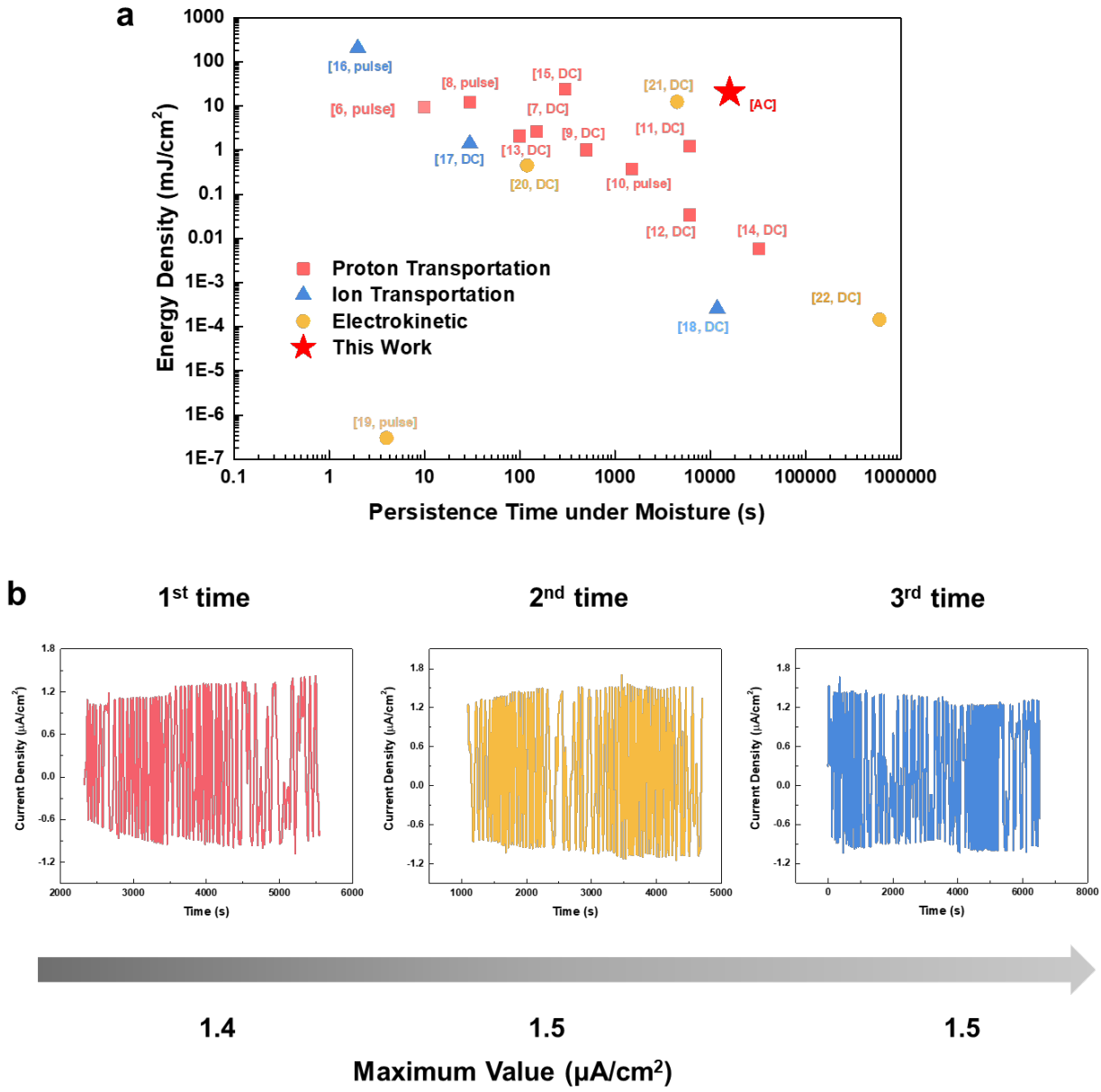

Fig. 6. (a) Comparison moisture-induced electric generators based on artificial materials in the operation period and energy density. This work has the long persistence time and high energy density among moisture-based energy harvesters, and these two parameters could be further improved by using other materials based on similar self-oscillation mechanisms. **(b)** The measured output current versus time results for a prototype energy harvester remain similar in three different independent tests in sequence.

The performances of various moisture-enabled energy harvesters using artificial materials are summarized in **Fig. 6**. In general, prior works have shown that moisture-induced energy harvesters can generate DC outputs. Here, autonomous surface potential oscillations are utilized to produce

alternating current (AC) or voltage outputs. For example, testing results show that an operation time of more than 15,000 seconds (about 4 hours), with an output energy density of 16.8 mJ/cm^2 can be achieved. This long operation time enables sustainable energy outputs under a relatively constant moisture source as the green energy supply. Moreover, the energy harvester is found to be reusable as shown in **Fig. 6b**, where a maximum current density values at around 1.5 μA/cm^2 has been found to be maintained for three independent tests.

A simple strategy to increase the output voltage of the energy harvester is to connect devices in series. As shown in **Fig. 7a**, the outputs of five devices (MEDSAH/AA ratio of 1/4) are rectified and connected in series to reach 2-Volt, which is high enough to light up an LCD (**Movie S2**). A demonstration toward practical usage is implemented in **Fig. 7b** by connecting five devices in series on the wall of a bathroom full of moisture during the shower time to light up an LCD. This is a direct validation that the moisture-enabled energy harvester can be used in naturally-produced high moisture environment to produce electrical energy.

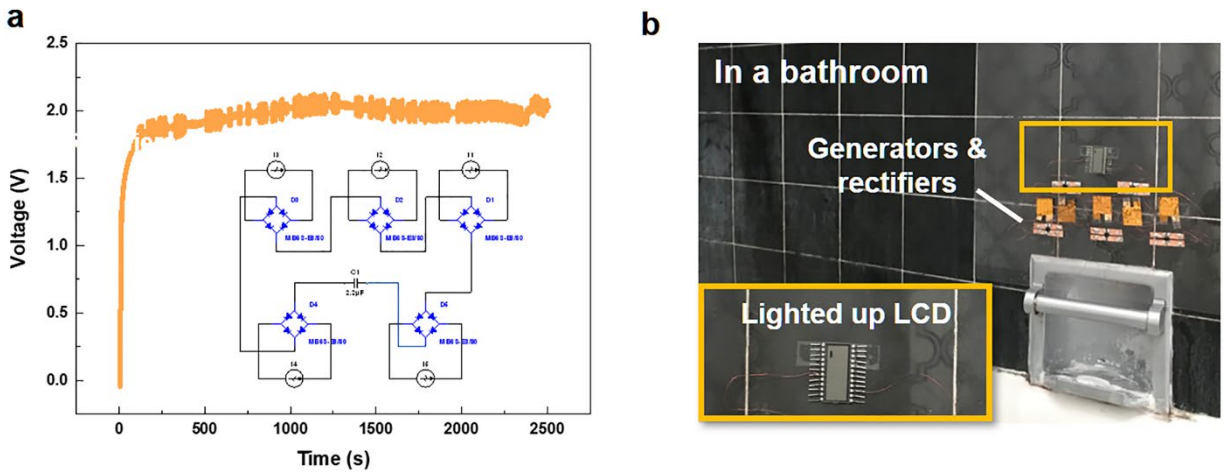

Fig. 7. Demonstrations of moisture-induced energy harvesters. **(a)** Rectified output voltage vs. time by five devices connected in series. Inset: the electrical circuit. **(b)** Lighting up an LCD in a bathroom with moisture from the shower. The inset shows the enlarged view of the system.

2.5 Experimental section

Polymer synthesis process: All chemicals are bought from Sigma-Aldrich and used without further treatment. First, the monomers and the initiator are weighted according to the designed ratio and solved in DI water with the weight ratio equals to 63 wt%. The initiator, APS, is 2 mol% compared with monomers. After fully mixed, the solution is poured into a plastic petri dish and heated at 50 ºC for 24 h. Since the polymers contain dynamic bonds – hydrogen bonds and ionic bonds, their mechanical properties are stable before and after the hydration processes (**Fig. S19**). A rinsing process in DI water is used to get rid of unreacted reactants.

Device fabrication: After the polymer synthesis process, an individual specimen is cut into 2×2 cm^2

pieces. A polyimide (PI) film of 20 μm in thickness is sputtered with 100-nm-thick Au as electrodes. The top electrode has 25 mechanically punched holes (diameter of 2 mm) to allow the exposure to moistures. Finally, the electrodes are adhered to the polymer structure to complete the device fabrication process.

Electric signal measurement: The electrical current is measured via a current amplifier (SR570), and the output voltage is measured by a Data Acquisition system (DAQ, National Instruments).

pH measurement: The pH sensor is fabricated *via* the electrodeposition of aniline as reported previously in the literature[49,50]. For the pH measurement, the top surface of the polymer is first dampened with ~100 μL of water. Then the pH sensor and an Ag/AgCl reference electrode (3 mol/L KCl) are attached to the top surface of the polymer and the open circuit potential between pH sensor and the reference electrode is measured with an electrochemistry workstation (Gamry Reference 600). The pH values are calculated using a calibration curve obtained from McIlvaine buffer solutions with pH value ranging from 2 to 5. The pH values of McIlvaine buffer solutions are pre-calibrated with a commercial pH meter (*Hanna Instruments, HI2210*). Table 1 shows the measured potential and its corresponding pH value. By linear fitting, it can be found that the reading potential has good linear relationship with pH with adjacent R square equals to 0.9942: $pH = \ 14.092 - 0.01545 * Reading$.

Table 1. Measured potential (Reading) and the corresponding pH values.

pH	Reading(mV)
2.51	746.3
3.57	686.4
4.47	622.2
4.78	600.7

Characterizations:

(1) EDX tests are performed on a Scanning Electron Microscope (Hitachi 2460 with KEVEX) at 40 keV and the dwelling time is 5 μs.

(2) ATR-FT-IR spectroscopy of dry and wet samples are performed on a Bruker ALPHA Platinum ATR-FT-IR spectrometer equipped with a single reflection diamond ATR module in the ambient atmosphere.

(3) The surface potential is measured using KPFM on an MFP-3D atomic force microscopy (AFM; Asylum Research, Santa Barbara, CA) with Ti/Pt-coated AC250TM-R3 (Oxford Instruments) AFM tip with a radius of ~28 nm, spring constant of ~2 N/m, and resonant frequency of ~70 kHz. All measurements are performed at atmospheric pressure, ~20 ℃, ~40 % of relative humidity.

2.6 Summary

In summary, a surface potential oscillation phenomenon in moisture-induced P(MEDSAH-co-AA) polymer has been characterized and an AC energy harvester has been demonstrated. Chemical reactions responsible for the autonomous potential oscillation behavior are analyzed and modelled by kinetic simulations to qualitatively characterize this phenomenon. By studying system dynamic equations and the stability matrix, it is found that the system has the chaotic nature and oscillates with hidden attractors to induce autonomous surface potential oscillation. A prototype energy harvester has a measured maximum short-circuit current density of 1.5 $\mu A/cm^2$ and maximum open-circuit voltage of 0.4 V with a long operation time up to 15,000 seconds in a moisture-rich environment to produce an energy density of 16.8 mJ/cm^2. As a practical application demo, an LCD is successfully lit up by connecting five energy harvesters in series to produce an output voltage of 2 Volts.

3. Thermoelectric energy harvesters based on an ionogel with ultra-high Seebeck Coefficient

3.1 Ionogel systems

The ionogel developed in this work has two unique features: (1) flexible and bendable; (2) the electrical conduction mainly by ions and the thermal conduction mainly by polymer structures. **Fig. 8a** illustrates these conduction paths, where the cations and anions move between the polymer chains along the temperature gradient with different mobility. For the material presented in this work, the mobility of cations is higher than that of ions. These different charge carriers will accumulate at the two ends of the material and induce charges on the electrodes to generate electricity. **Fig. 8b** shows the key mechanism of the dynamic bonds to induce the self-healing property of the material. The material satisfies two requirements of a self-healable system [52]: (1) the free ions inside the ionogel have ion-dipole interactions with the polar functional groups on the polymer chains to form plenty of dynamic bonds, and (2) the organic solvent remaining in the ionogel material makes the polymer chains movable. Different electrical/thermal conduction paths in ionogel make it possible to design and construct materials with high electrical conductivity but low thermal conductivity for large zT values. On the other hand, the self-healing property of the ionogel makes it possible for operations under large deformations such as applications for flexible devices and wearable systems.

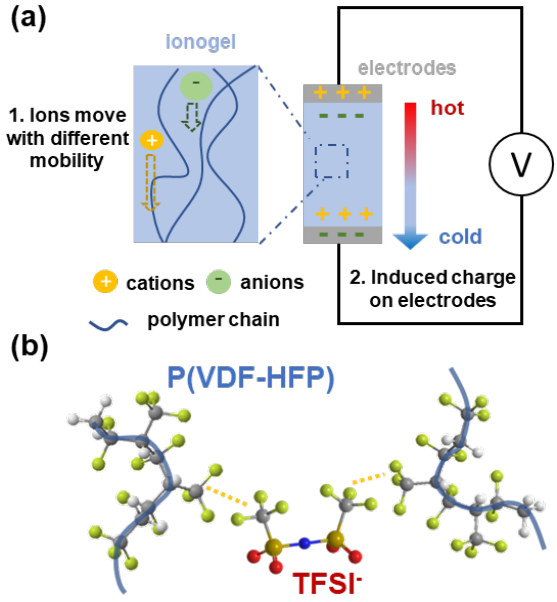

Fig. 8. (a) Schematics illustrating the ionogel used in the thermoelectric generator and different electrical and thermal conduction paths in ionogel make it possible to design and construct materials with high electrical conductivity but low thermal conductivity for large zT values. **(b)** The ion-dipole interaction inside the ionogel leads to its self-healing property.

3.2 Preparation of the ionogel

The ionogel used in this work is prepared as described in **Fig. 9**. A fluoroelastomer, poly(vinylidene fluoride-*co*-hexafluoropropylene) (P(VDF-HFP), 3M™ Dyneon™ Fluoroelastomer FC 2230), and one organic salt bis(trifluoromethane) sulfonimide lithium salt (LiTFSI, Sigma-Aldrich), are mixed with the weight ratio equal to 3:2. The mixture is dissolved by the solvent: *N, N*-dimethylformamide (DMF) and acetone (volume ratio = 3:7, both from Sigma-Aldrich). After getting a clear and homogeneous solution, the mixture is poured into a mold and put under vacuum and heated to 80°C for 24 hours to get rid of extra solvent. It is worth mentioning that DMF is a solvent with a high boiling point at 153°C, and low vapor pressure at 350 Pa under the ambient environment. These properties make it possible for materials to remain in the ionogel to prevent the crystallization of LiTFSI. With free cations (Li^+) and anions ($TFSI^-$) staying inside the ionogel, the material can be electrically conductive.

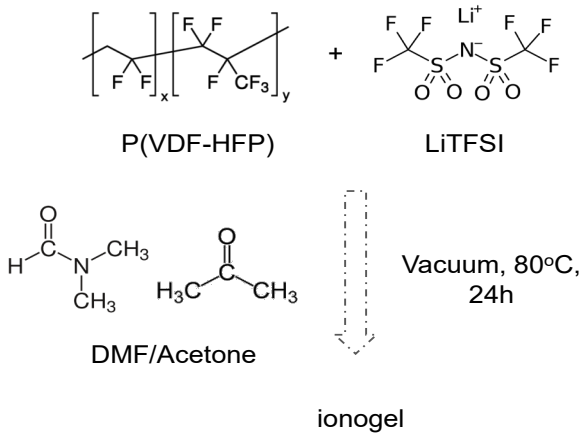

Fig. 9. Preparation method used in this research.

3.3 Diffusion coefficient simulation

The diffusion coefficients of anions and cations are simulated through molecular dynamics (MD). The simulation is performed on large-scare atomic/molecular massively parallel simulator (LAMMPS). The system consists of 84,600 atoms totally – 600 LiTFSI, 9000 DMF and 100 polymer chains, which corresponds with the ratio of the ionogel compositions (**Fig. 10a**). The inter-atom interaction is described using optimized potentials for liquid simulations (OPLS) force field. Particularly, the OLPS-united atoms (UA) model [53] is adopted to describe DMF molecules, meaning that DMF is treated as one atom. Other molecules are described by the OLPS-all atoms (AA) model, meaning that the different atoms on one molecule are treated separately. The model of $TFSI^-$ is modified and optimized according to the previously reported work [54].

After the construction, the system is relaxed under the restriction of constant molecular number, constant pressure, and constant temperature, to get its initial configuration. After that, radical

distribution function analysis is performed on Li^+ and $TFSI^-$ to calculate the coordination of ions/molecules, which influence the volume of ions in the real situation and their diffusion coefficients. The mean square distances (MSD2) of anions and cations are simulated under different temperatures from 285K to 310K (**Fig. 10b**). The diffusion coefficients (D) can be derived through the fitting curve of MSD^2 and time (t) according to the equation below:

$$MSD^2 = 6Dt + Const \qquad (3)$$

Fig. 10c summarizes the diffusion coefficients of Li^+ and $TFSI^-$ in the temperature range. Clearly, the diffusion coefficient of Li^+, which is $6{\sim}10 \times 10^{-12}\ m^2/s$, is much larger than that of $TFSI^-$ (less than $2 \times 10^{-12}\ m^2/s$).

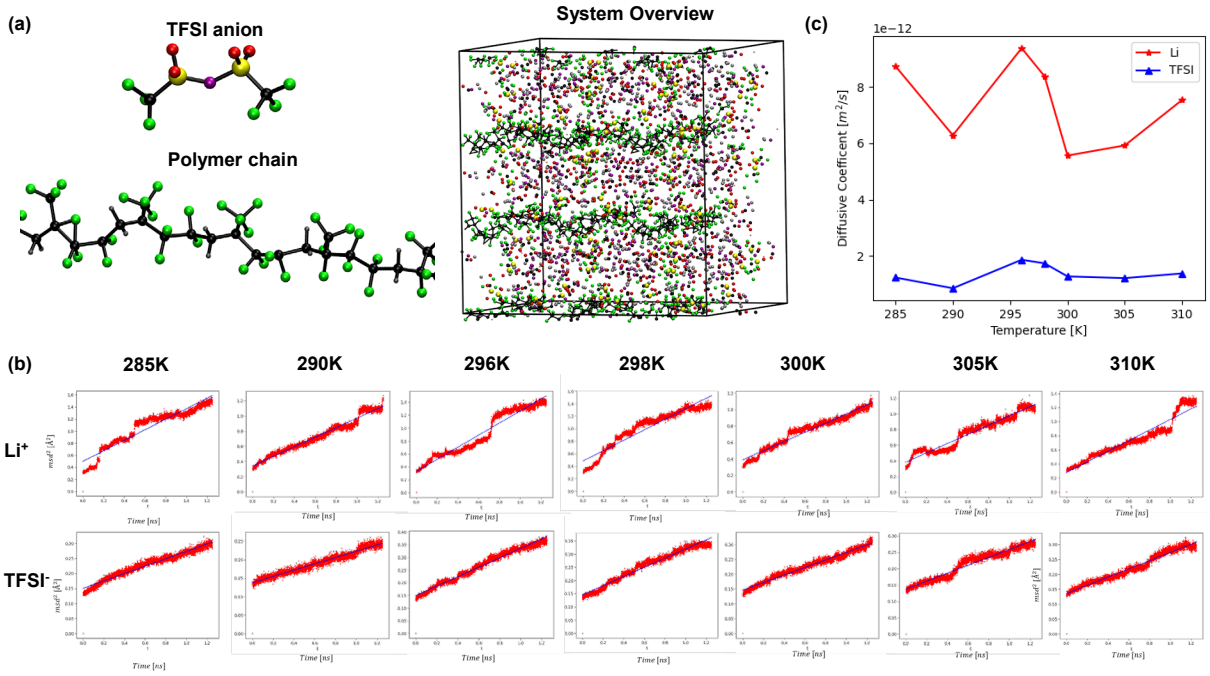

Fig. 10. (a) The model and the system used in the MD simulation. **(b)** The simulation results of MSD^2 of Li^+ and $TFSI^-$ at different temperatures (from 285K to 310K). **(c)** The diffusion coefficients of anions and cations under different temperatures. Li^+ has much larger diffusion coefficients in the temperature range from 285K to 310K as compared with those of $TFSI^-$.

3.4 Device assembly and structure

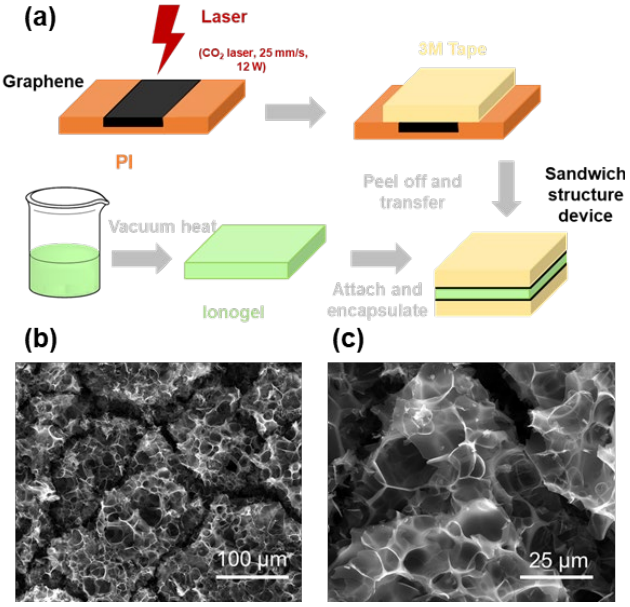

Fig. 11. (a) The fabrication process of the thermoelectric generator. **(b, c)** SEM photographs of the LIG electrodes showing porous structures under different magnification scales.

The structure of the thermoelectric generator is shown in **Fig. 11a**, where the ionogel is used as an electrolyte. The electrodes are made of laser-induced graphene (LIG) with a dimension of 2 cm × 1 cm for the prototype device. The LIG is fabricated by a direct laser printing (CO_2 laser, *Tek Motion*, with a wavelength of 10.6 μm) process on a polyimide (PI) film. The laser power is 12 W and the scan rate is 25 mm/s. The LIG has a porous structure as shown in **Fig. 11b** and **11c** to result in electrodes with very high specific surface areas for the storage of ions in the energy harvester application. The LIG is transferred to the 3M™ 4910 VHB via a double-sided tape by simply pasting it on the LIG and peeling the tape off. Afterward, the electrodes are attached to both sides of the ionogel.

3.5 Device performance

The thermal energy harvester utilizes the differences in the directional movements of cations and anions of different mobilities [55]. Specifically, both the cations and the anions will move due to temperature gradients and carry different electrical charges. In the proposed material system, Li^+ has a size of about 1 Å and $TFSI^-$ has a size of about 3.9 × 8.0 Å [56]. Furthermore, $TFSI^-$ has more polar interactions with the polymer matrix such that the mobility of the cations is much larger than that of the anions. Therefore, there will be an electric potential difference between two electrodes under a temperature gradient. **Fig. 12a** shows the voltage outputs generated by the prototype device under different temperature gradients. It is noted that the relationship is nonlinear as the competition process of anions and cations is rather complex. In general, the temperature increases will result in the large

movements of more anions with higher mobility for increased output voltage as shown.

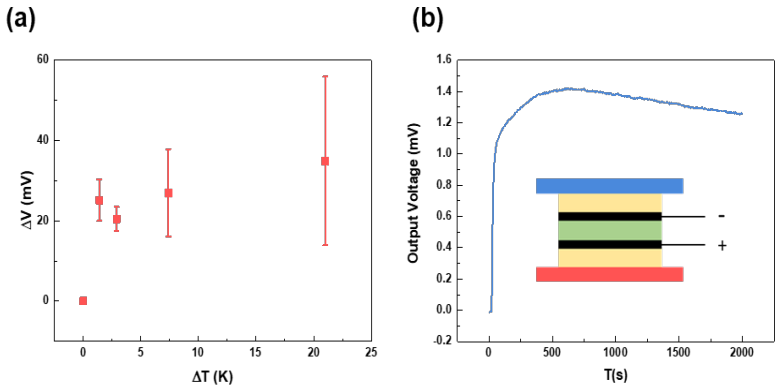

Fig. 12. (a) The open-circuit output potential under different temperature gradient (using aluminum electrodes). **(b)** The output voltage of the energy harvester device under ΔT = 4.7 K. The inset shows the testing platform (the red part is the heat source and the blue part is the heat sink). The 3M tape is a thermal insulator such that the real temperature gradient of the ionogel layer is expected to be much lower than 4.7 K to result in low voltage outputs.

Table 2. Comparison of the Seebeck coefficient among this work and other materials.

Materials	Seebeck Coefficient (μV/K)
This work	~7068 (material), 298 (device), at ΔT = 4.7K
silicide	-175 (material)
Mn oxide	~ -200 (material)
Co oxide	~245 (material)
Antimony	47 (material)
Cadmium, tungsten	7.5 (material)

The voltage output of the whole device is measured by its open-circuit voltage (*Gamry Reference 600*) with the heat source on one side and the heat sink (both are *TEC 1-12706 SR*, powered by a current source, *TEKPOWER TP300ST*) on the other side. The measured temperature difference between the heat source and the heat sink is 4.7 K. Since the 3M tape acts as a thermal insulator such that the temperature gradient on the ionogel layer is much lower than 4.7 C. Nevertheless, the output voltage curve (**Fig. 12b**) still shows an obvious increase due to the temperature changes. Under this setup, the maximum voltage output reaches 1.4 mV and the Seebeck coefficient is 298 μV/K. The apparent Seebeck coefficient is much lower than that of the ionogel as the 3M tape blocks heat transfer processes. After the first 500 s, the voltage output gradually decreases slightly as anions ($TFSI^-$), which carries different charge with low mobility, are also moving from the heat source side to the heat sink side. However, since the anions and the cations have different mobility, voltage outputs might continue for 12,000 s by extrapolating the curve. **Table 2** compares the Seebeck coefficient between this work and other traditional thermoelectric materials (data from one review paper [57]).. It can be found that

the Seebeck coefficient of the ionogel is much larger than those of traditional materials.

The whole device is also flexible and self-healable, which can be demonstrated in **Fig. 13a-c**. **Fig. 13a** is the photograph of the initial device, and it can be bent with a radius of 1.25 cm (**Fig. 12b**). The self-healing ability of the device has been proved by cutting through the sample and putting two parts under the ambient environment tightly for 24 hours for the self-healing process and the red dash-line shows the original cutting path. The cyclic voltammetry (CV) measurements are conducted on the device at the different statuses on the electrochemical workstation (*Gamry Reference 600*). It can be found that the CV curves before and after mechanical bending of the device are almost the same. The enclosed area of the CV curve before and after the self-healing process is less than 10% to validate excellent device performance after the self-healing process. **Fig. 13d** shows the device behavior during the charging process by applying a temperature gradient of *2 K* and the constant current discharging process after removing the heat source.

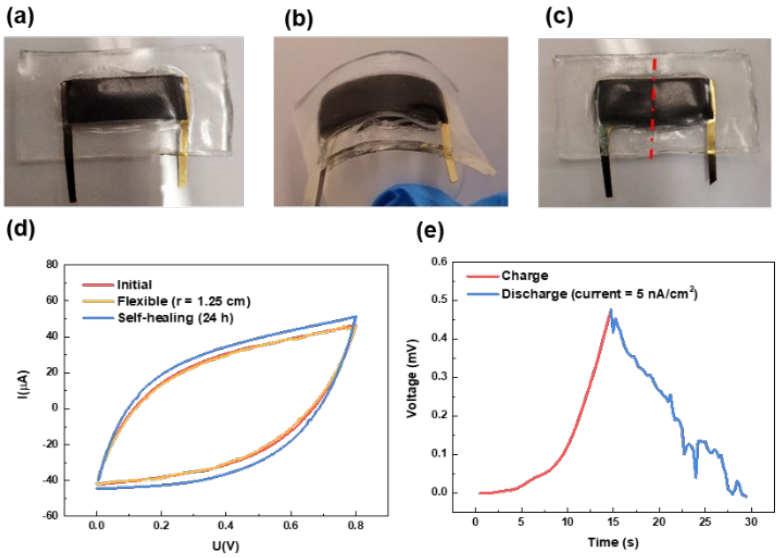

Fig. 13. Photographs of the devices: **(a)** initial state; **(b)** good bending flexibility with the radius of curvature of 1.25 cm; **(c)** after cutting the material and self-healed in the ambient environment for 24 h with the red dash line showing the healed interface. **(d)** The cyclic voltammetry curves of the device in the above three situations. **(e)** The charge (ΔT = 2 K) and discharge (current density = 5 nA/cm^2) curve of the device.

3.6 Self-healing property

The self-healing ability of the device comes from two aspects: the self-healing ability of: (1) the ionogel electrolyte; and (2) the electrodes.

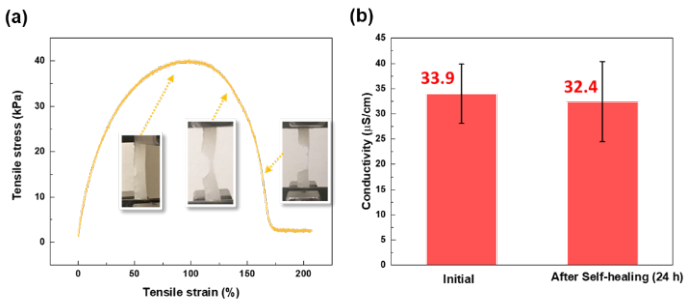

Fig. 14. (a) The result of the extension test (Instron) of the ionogel. The insets are the photographs of the ionogel during the test under different tensile strain. **(b)** The comparison of the ionogel electric conductivity before and after the self-healing process (100% cut through and self-healed under the ambient environment for 24 h.

Fig. 14a shows the strain-stress curve of the ionogel under the strain rate of 0.2 %/s. The ionogel can be stretched to 1.9 times of its original length. At this range, the elastic modulus is about 94 kPa. With strain further increased, a notch is formed and extended from one side of the ionogel to another side and leads to failure. The electrical conductivity of the ionogel is tested through electrochemical impedance spectroscopy (EIS) on the electrochemical station (*Gamry Reference 600*). The ion conductivity of the ionogel is 33.9 μS/cm (**Fig. 14b**), which is at the same level as traditional polyvinyl alcohol - orthophosphoric acid (PVA-H_3PO_4) electrolyte [58].

The ionogel is self-healable without heat or other treatments. A whole device is cut into two pieces and placed together tightly in the ambient environment for one day. It is found its electric conductivity can recover to 32.4 μS/cm (**Fig. 14b**) with a slightly decreased value of only about 4%. The self-healing process is examined under the scanning electron microscope (SEM, *FEI Quanta*) as shown in **Fig. 15**. The re-grown part (inside the yellow dash rectangle) can be seen clearly at the healed interface, directly proving the self-healing process inside the ionogel.

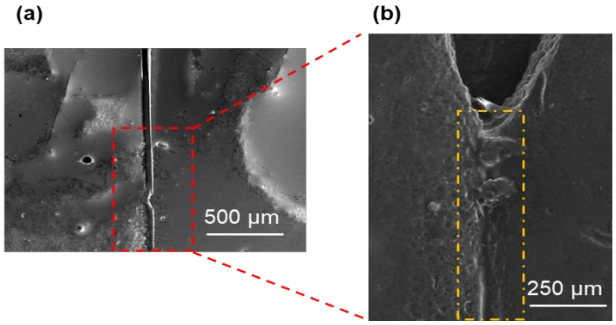

Fig. 15. SEM of the ionogel showing the self-healing process. **(a)** the photograph of the interface of two parts; **(b)** an enlarged view of the self-healing interfaces (yellow dash rectangle).

The self-healing ability may come from the polar interaction between the anions and the functional groups of the polymer backbone [59] (**Fig. 9b**). Both the polymer matrix and the anions contain

fluorine atoms, which have the highest electronegativity among all elements, leading to high polarity of anions and -CF_3. These polar interactions are dynamic and reversible and the anions serve as "bridges" between polymers, connecting polymers back again in the self-healing process.

Although LIG does not have the self-healing ability, the 3M tape is selected as the electrode substrate for the known self-healing property, which makes it possible to achieve a self-healable device. **Fig. 16** shows the SEM results of the electrodes after the self-healing process. The electrodes were cut through first and put back together for 24 hours under room temperature. The healing interfaces (yellow dash lines) can be hardly observed from SEM photographs. The initial sheet resistance of the electrode is 280 Ω/□ and it increases to 317 Ω/□ after the self-healing process, which is an increment of 13% (**Fig. 16d**).

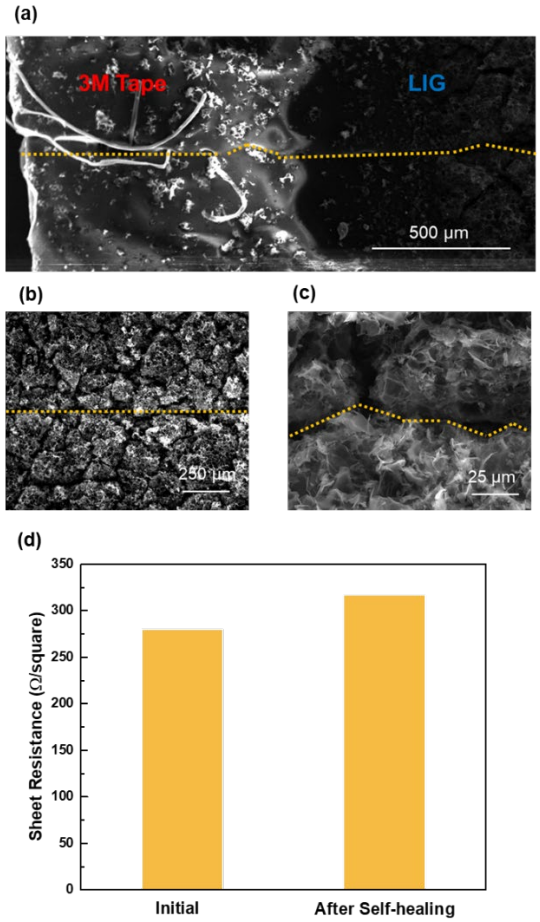

Fig. 16. SEM results of **(a)** and **(b, c)** LIG on a different scale, after the self-healing process (100% cut through and self-healed in the ambient environment, 24 h). Yellow dash lines highlight the healing interfaces. **(d)** The comparison of the electrode sheet resistance before and after the self-healing process.

3.7 Summary

In this work, we successfully designed and fabricated a thermoelectric energy harvester based on ion-conductive and self-healable ionogel. The whole device shows a high Seebeck coefficient at 298 μV/K, which is comparable and even much higher than those of traditional thermoelectric materials. The whole device is also flexible and self-healable with the performance almost unchanged in different statuses.

4. Conclusions

A moisture electric generator and a thermoelectric harvester based on polymers are achieved. They show promising potential on the applications in renewable energy field. The moisture electric generator is based on the polymers, P(MEDSAH-co-AA), which has a unique phenomenon of moisture-induced electrical potential oscillations during the diffusion of water molecules. Chemical reactions are modelled by kinetic simulations while system dynamic equations and the stability matrix are analyzed to show the chaotic nature of the system which oscillates with hidden attractors to induce the autonomous surface potential oscillation. Using moisture in the ambient environment as the activation source, this self-excited chemoelectrical reaction could have broad influences and usages in surface-reaction based devices and systems. As a proof-of-concept demonstration, an energy harvester is constructed and achieved the continuous energy production for more than 15,000 seconds with an energy density of 16.8 mJ/cm^2. A 2-Volts output voltage has been produced to power a liquid crystal display toward practical applications with five energy harvesters connected in series.

The thermoelectric energy harvester based on an ion-conductive ionogel. It has three distinctive features as compared with the state-of-art systems: (1) self-healable in both the material and device operations under large deformations; (2) ultrahigh Seebeck coefficient with the measured value of 7068 μV/K for the material, and 298 μV/K for a prototype energy harvester in operations; and (3) stable performances under large bending states with little changes. As such, this energy harvester could find potential applications by further packaging and design in wearable devices to convert the temperature differences between human body/skin and environment to electricity.

Supplemental Information

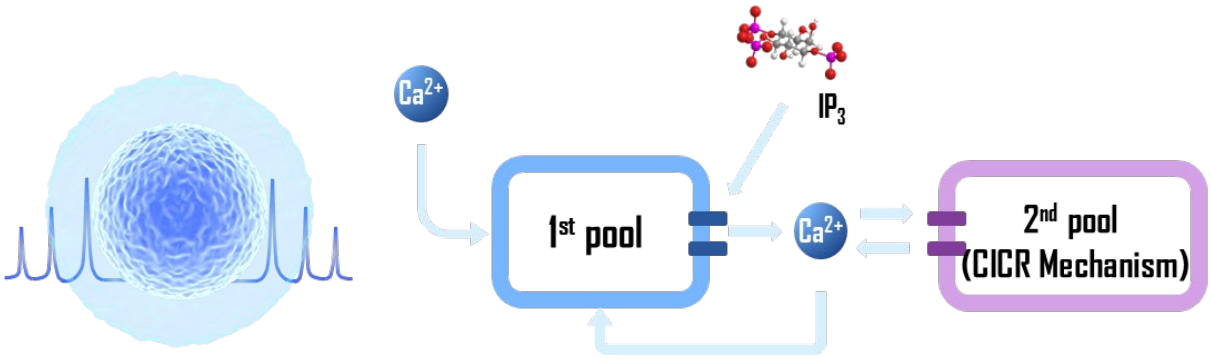

Fig. S1. A schematic diagram illustrating the Calcium-induced Ca^{2+} release (CICR) process to induce the Ca^{2+} concentration oscillation in a living cell.

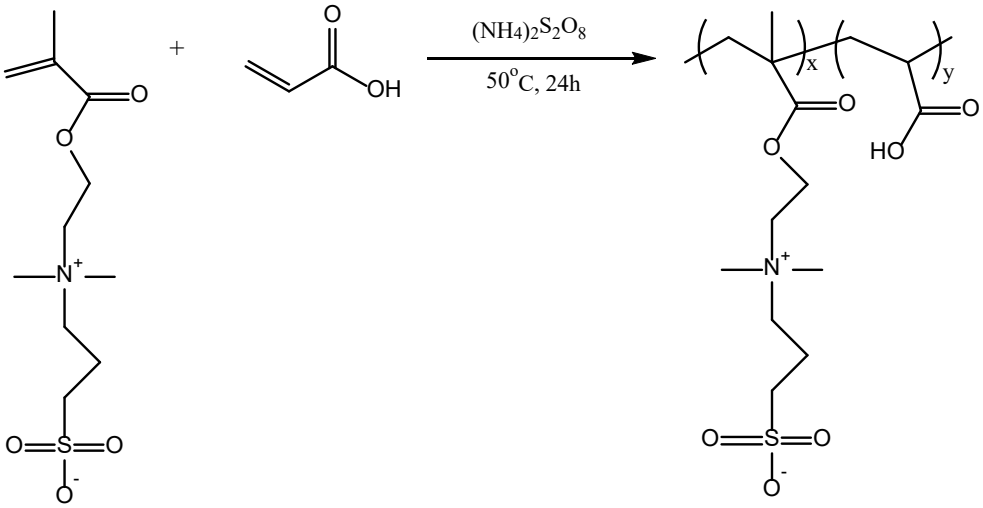

Fig. S2. The synthesis process of P(MEDSAH-co-AA) polymer.

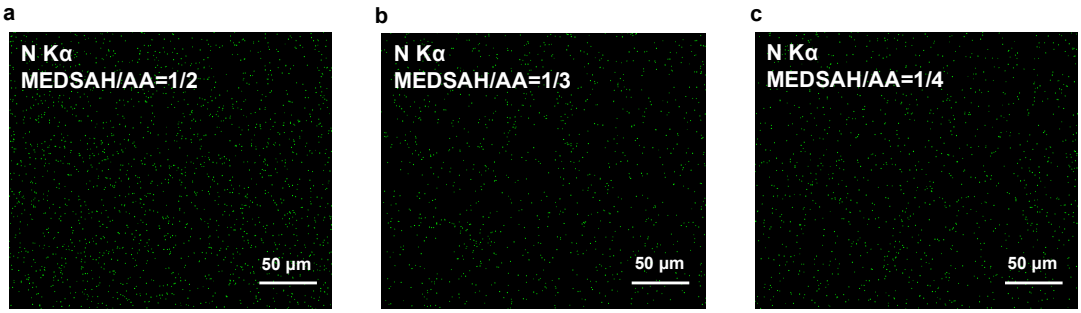

Fig. S3. The EDX results of polymers with three different compositions: MEDSAH/AA= (a) 1/2; (b) 1/3; and (c) 1/4. Green spots are nitrogen.

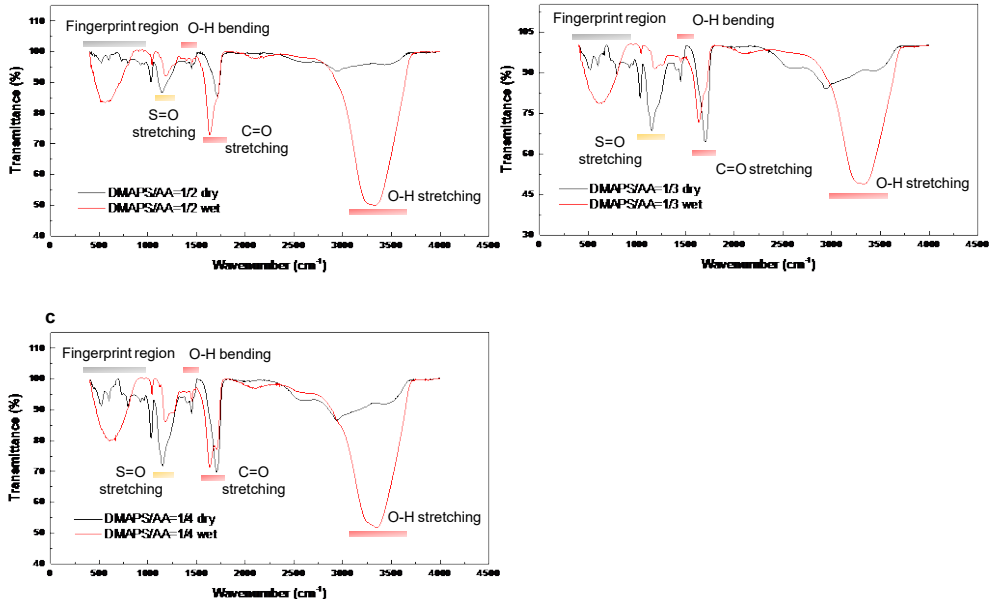

Fig. S4. ATR-FT-IR results of dry and wet P(MEDSAH-co-AA) polymers with different compositions: (a) MEDSAH/AA=1/2; (b) MEDSAH/AA=1/3; (c) MEDSAH/AA=1/4.

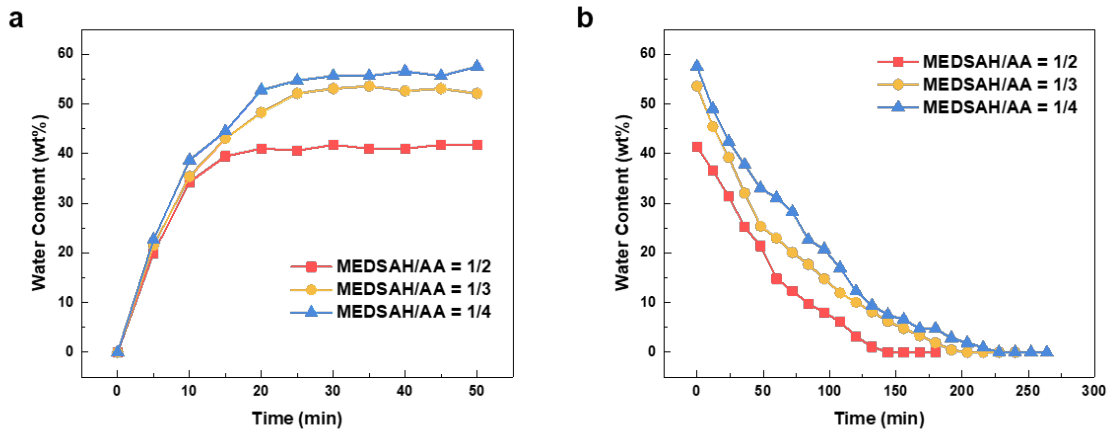

Fig. S5. The water content of polymers with different compositions during: (a) the hydration and (b) the dehydration process. It can be found that the polymer containing more -COOH can absorb more moisture at a faster speed in (a) and maintain higher moisture concentrations in (b).

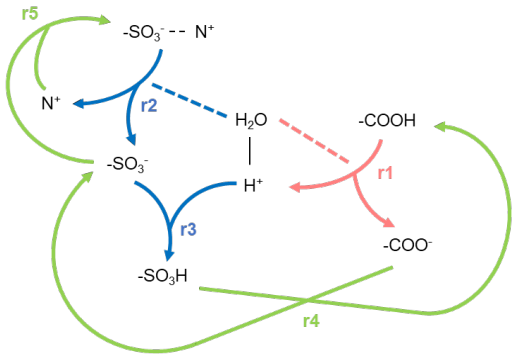

Fig. S6. Summary of the proposed "proton oscillation" mechanism by different chemical reactions: r1 (positive feedback in the red color), r2 and r3 (negative feedback in the blue color), r4 and r5 (returning to initial state in the green color). The dash lines suggest the participation of water molecules in r1 and r2.

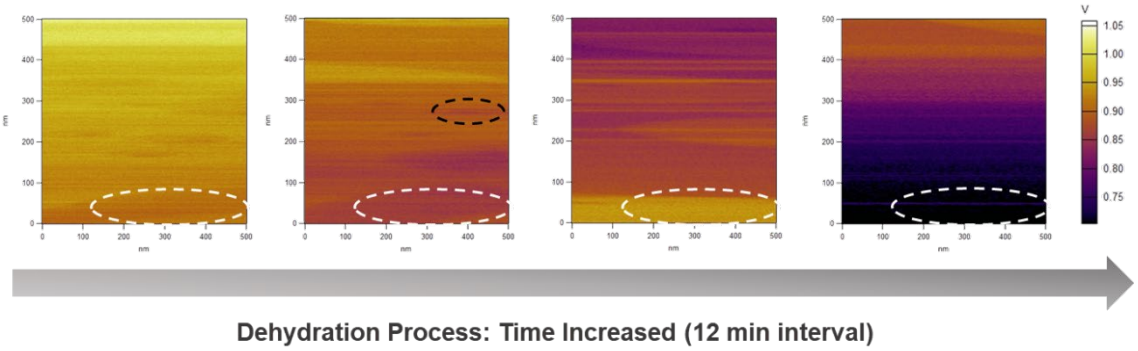

Fig. S7. Kelvin probe force microscopy (KPFM) for surface potential oscillation results at the same surface location of a prototype polymer during the moisture activation and dehydration process. Each test needs about 12 minutes to complete and the white elliptical area highlights the local surface potential oscillations. Other areas have also experience surface potential oscillations with slightly different surface potential values.

After saturating the P(MEDSAH-co-AA) polymer with water at 41 wt%, the Kelvin probe force microscopy (KPFM) is used to measure the surface potential at a fixed area of 500×500 nm^2 as depicted in **Fig. S7**. In general, the average surface potential is found to gradually decrease over time. However, the time-varying oscillations in a short period of time are also observed. For example, in the white elliptical area in **Fig. S7**, the surface potential is found to oscillate during a period of every 12 minutes (this test is limited by the scanning speed of the KPFM) from 0.92 V, 0.85 V, 0.96 V, to 0.74 V, sequentially. Even though limited by scanning speed, KPFM analysis shows the general oscillation tendency of the surface potential. The other areas also experience similar but different surface potential oscillations as observed.

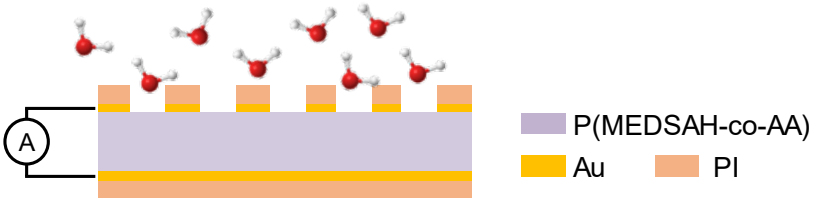

Fig. S8. The cross-sectional view of the energy harvester device.

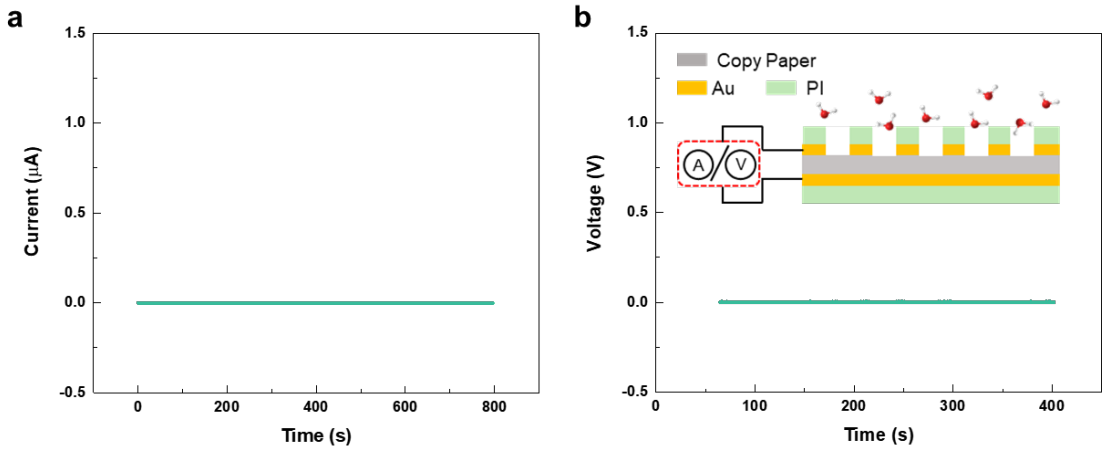

Fig. S9. The (a) close-circuit current and (b) open-circuit voltage vs. time results of a prototype device by using a copy paper instead of the P(MEDSAH-co-AA) polymer. No visible electrical outputs are identified.

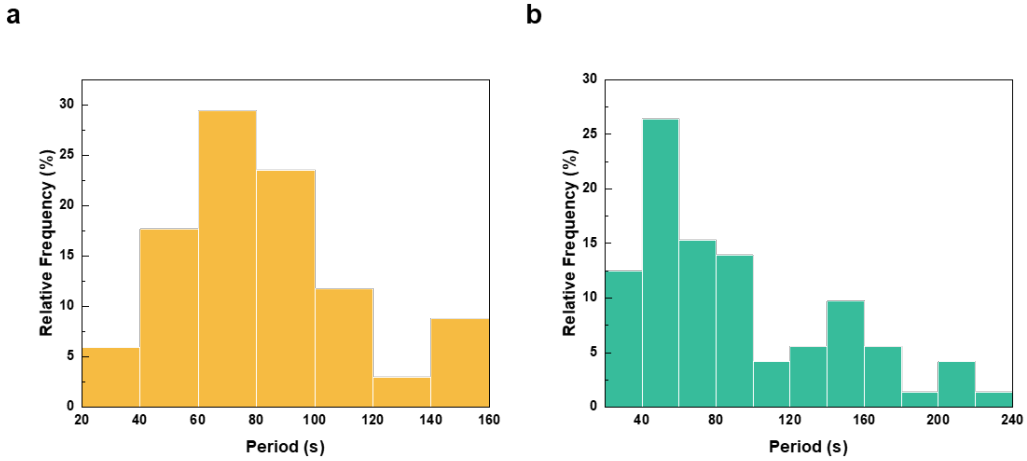

Fig. S10. The histogram of energy generation cycle period of a prototype energy harvester: (a) energy generation period; and (b) low electrical output periods (noises).

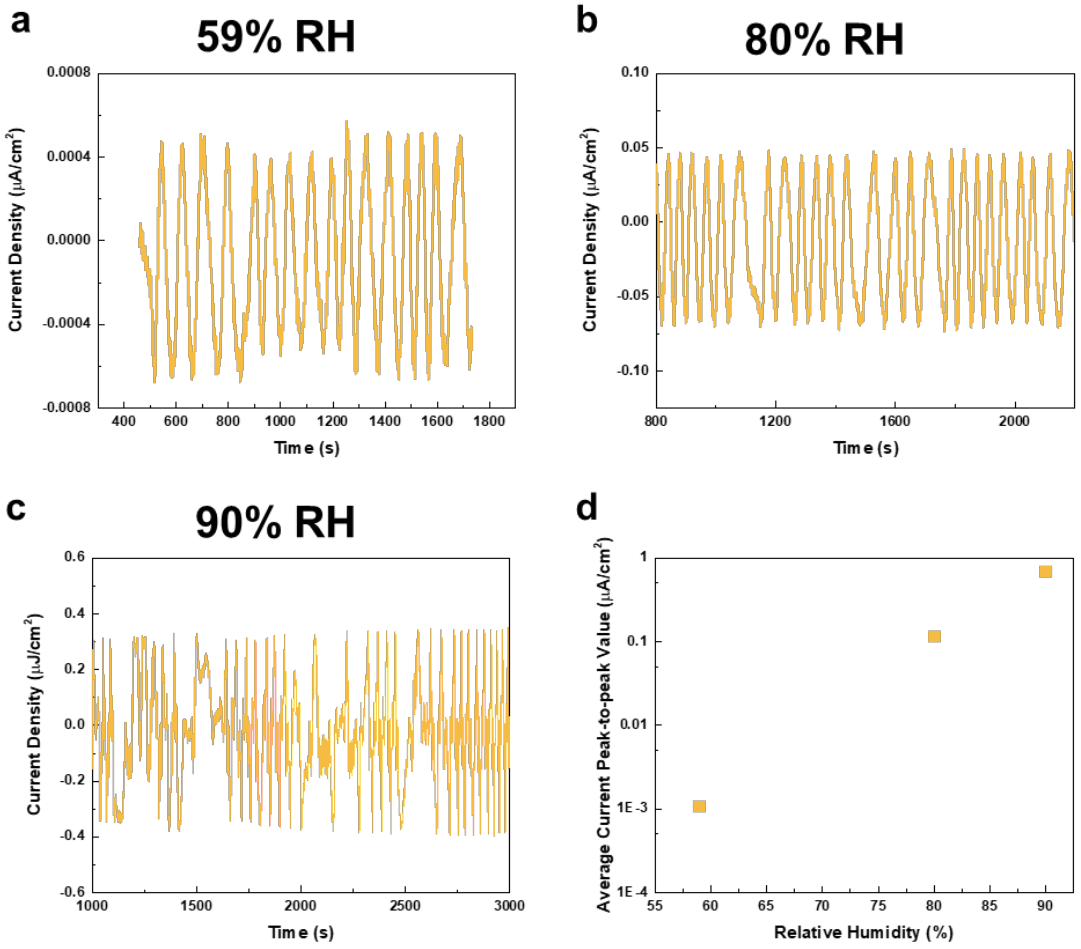

Fig. S11. The measured output current density versus time of the prototype energy harvester under various humidity levels of (a) 59% RH, (b) 80% RH, and (c) 90% RH. (d) Average peak-to-peak current density versus relative humidity.

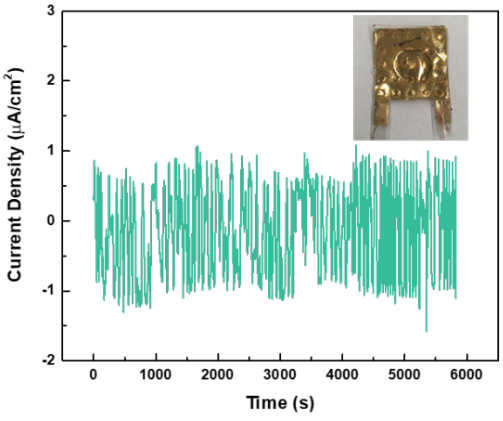

Fig. S12. The output current vs. time plot by placing a water droplet on the device.

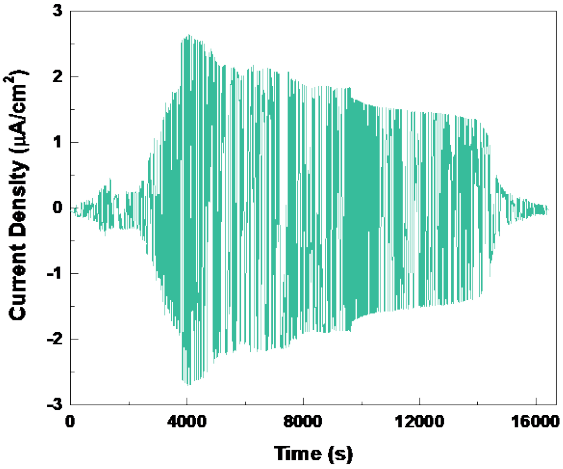

Fig. S13. The current output under continuous moisture feeding without the dehydration process.

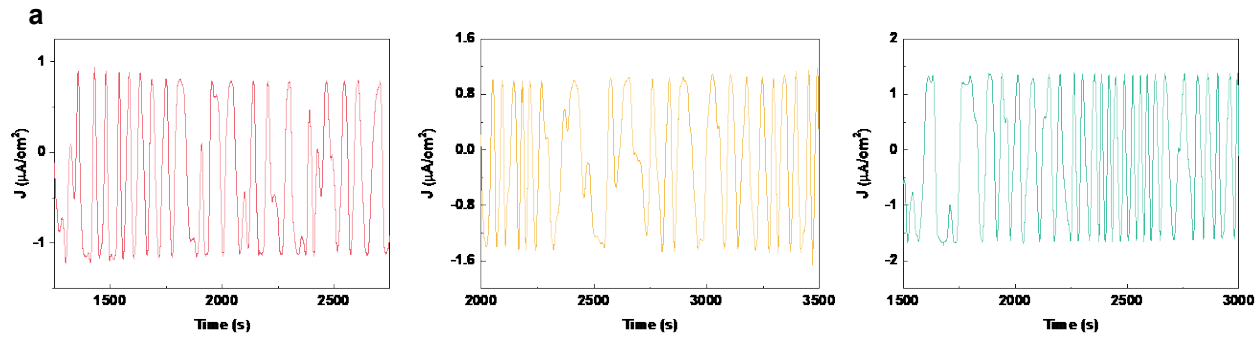

Fig. S14. Output current density versus time of energy harvesters with different polymer compositions: (a) MEDSAH/AA=1/2; (b) MEDSAH/AA=1/3; (c) MEDSAH/AA=1/4.

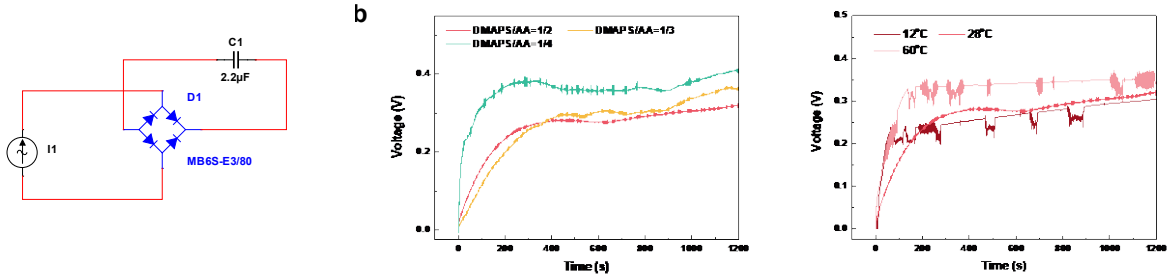

Fig. S15. (a) The electrical circuit used to charge the capacitor for measuring the DC output voltage; (b) voltage versus time plot of energy harvesters with different polymer compositions ("reference" refers to the outside noise); (c) voltage versus time plot of the energy harvester (MEDSAH/AA=1/4) under different working temperatures.

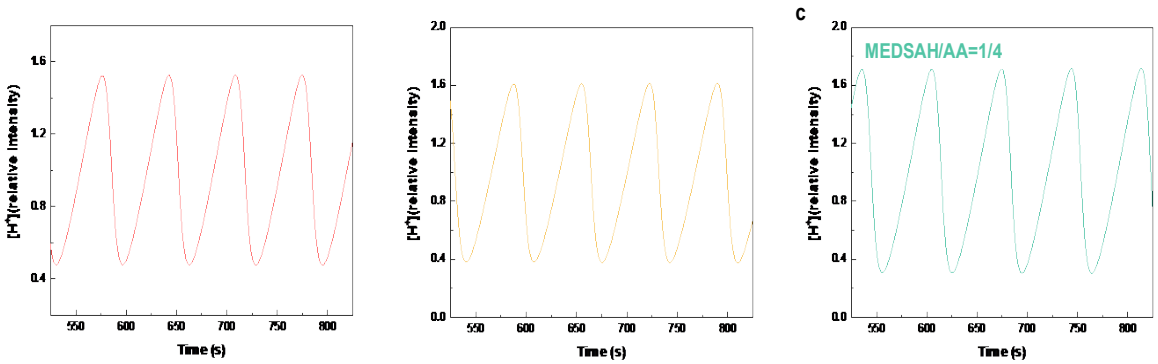

Fig. S16. Proton oscillation simulation results of polymers with different compositions: MEDSAH/AA= (a) 1/2; (b) 1/3; (c) 1/4.

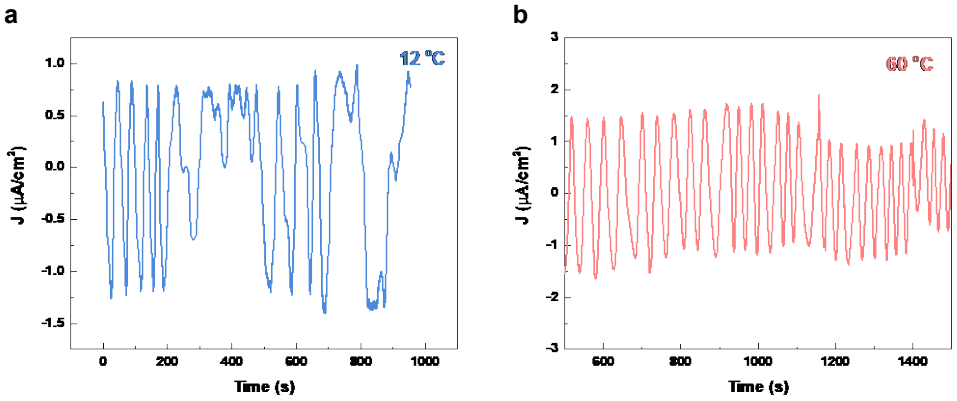

Fig. S17. Measured output current versus time of the energy harvester (MEDSAH/AA=1/2) at (a) 12 °C and (b) 60 °C.

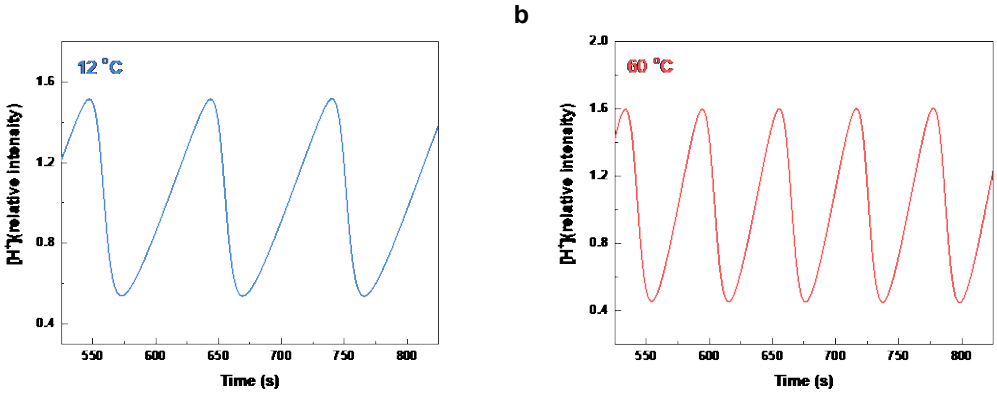

Fig. S18. Simulation results of proton oscillation versus time for polymer (MEDSAH/AA=1/2) under (a) 12 °C and (b) 60 °C.

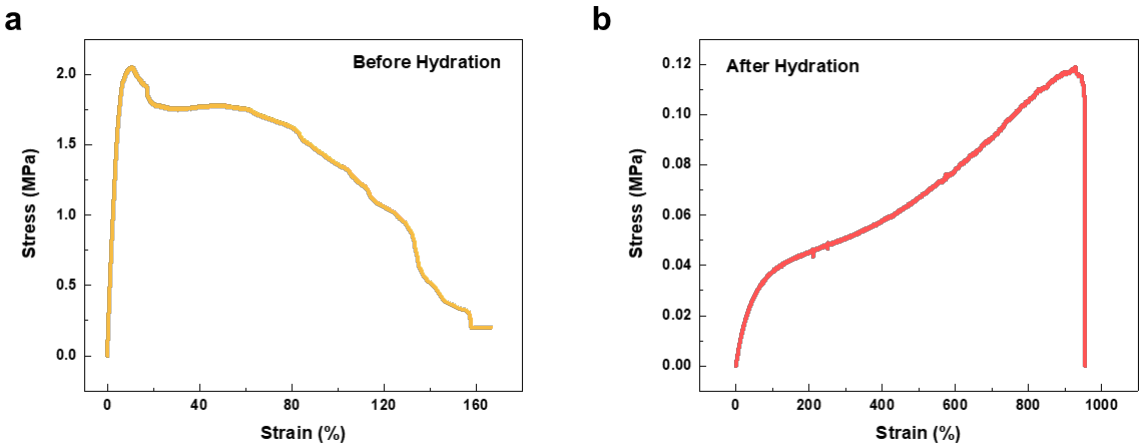

Fig. S19. The measured stress-strain curves of the polymer (a) before and (b) after the hydration process. The calculated Young's modulus values are 30.6 MPa and 66.8 kPa before and after hydration, respectively.

Supporting Explanation 1: Kinetic Simulation:

Kinetic analysis of the chemical reactions is performed based on the 5 key reactions in the system:

$r_1: -COOH == H^+ + -COO^-$

$r_2: -SO_3^-N^+ == -SO_3^- + -N^+$

$r_3: -SO_3^- + H^+ == -SO_3H$

$r_4: -SO_3H + -COO^- == -SO_3^- + -COOH$

$r_5: -SO_3^- + -N^+ == -SO_3^-N^+$

The reaction rate constants are added as:

$v_{r1} = k_1[-COOH]$

$v_{r2} = k_2[-SO_3^-N^+]$

$v_{r3} = k_3[-SO_3^-][H^+]$

$v_{r4} = k_4[-SO_3H][-COO^-]$

$v_{r5} = k_5[-SO_3^-][-N^+]$

Therefore, the concentration gradient of each species with respect to time can be expressed as:

$$\frac{d[H^+]}{dt} = k_1[-COOH] - k_3[-SO_3^-][H^+] \quad (1)$$

$$\frac{d[-COOH]}{dt} = -k_1[-COOH] + k_4[-SO_3H][-COO^-] \quad (2)$$

$$\frac{d[-SO_3^-]}{dt} = k_2[-SO_3^-N^+] - k_3[-SO_3^-][H^+] + k_4[-SO_3H][-COO^-] \quad (3)$$

$$\frac{d[-SO_3^-N^+]}{dt} = -k_2[-SO_3^-N^+] + k_5[-SO_3^-][-N^+] \quad (4)$$

Furthermore, $[-N^+]$, $[-SO_3H]$ and $[-COO^-]$ are corelated by the conservation of matters:

$[-N^+] + [-SO_3^-N^+] = [-SO_3^-N^+] + [-SO_3H] + [-SO_3^-] = c_{N+SO3-}$

$[-COOH] + [-COO^-] = c_{carboxylic\ acid}$

The concentration of water, $[H_2O]$, is controlled by v_{in} and v_{out} as:

$$v_{in} = v_{out}\frac{[H^+]}{[H^+]_0}$$

where $[H^+]$ is the concentration of hydrogen cation and $[H^+]_0$ is the initial concentration. The concentration of water versus time can be expressed as:

$$\frac{d[H_2O]}{dt} = -v_{out} + v_{in}\frac{[H^+]}{[H^+]_0} \quad (5)$$

The water concentration affects the breaking of ionization bonds such that a factor is introduced in the reaction rate constant of r2 when the concentration of water, [H_2O], is lower than the threshold value $c_{threshold}$:

$$k_2 = \begin{cases} e^{-0.5(c_{threshold}-[H_2O])}\,k_2^0, & when\ c_{threshold} > [H_2O] \\ k_2^0, & when\ c_{threshold} \le [H_2O] \end{cases} \quad (6)$$

To numerically solve the differential equations (1)-(5), the explicit 1st-upwind scheme is adopted:

$$\frac{df}{dt} \approx \frac{f(t+\Delta t) - f(t)}{\Delta t} \quad (7)$$

By matching with experimental data, an optimal set of constants: $k_1 = 0.0000962$, $k_2^0 = 0.0949$, $k_3 = 0.1118$, $k_4 = 0.0871$, $k_5 = 0.0936$, timestep $\Delta t = 0.01$, $v_{in} = 0.94$, $c_{threshold} = 200$ have been identified for the system, while c_{N+SO3-} and $c_{carboxylic\ acid}$ varies according to different proportions of the total mass which is fixed as a constant at 150×10^5. Other sets of constants will produce different results in operation periods which deviate more from experimental observations. For example, by setting $k_1 = 0.000163$, $k_2^0 = 0.1606$, $k_3 = 0.1892$, $k_4 = 0.1474$, $k_5 = 0.1584$, the oscillation period is decreased to 57s. By setting $k_1 = 0.000074$, $k_2^0 = 0.073$, $k_3 = 0.086$, $k_4 = 0.067$, $k_5 = 0.072$, the oscillation period is increased to 97s. Table S1 summarizes these results.

Table S1. Summary of the kinetic constants

Period (s)	$\mathbf{k_1}$	$\mathbf{k_2^0}$	$\mathbf{k_3}$	$\mathbf{k_4}$	$\mathbf{k_5}$
57	0.000163	0.1606	0.1892	0.1474	0.1584
70	0.0000962	0.0949	0.1118	0.0871	0.0936
97	0.000074	0.073	0.086	0.067	0.072

The initial concentration of H^+, $[H^+]_0$ has a positive correlation with $c_{carboxylic\ acid}$ and other initial concentration is set as follows:

$$[-SO_3^-]_0 = 0$$
$$[H_2O]_0 = 170$$

The calculation script is written in python3 and resulting data are normalized by the initial proton concentration. Based on experimental results, the oscillation period is adjusted to about 70 s, by adjusting kinetic constants. It is also found that the oscillation period has different sensitivity on the kinetic constants. For example, k_2^0 and k_4 have minimum influences on the oscillation period (**Fig.**

S20), while k_1, k_3 and k_5 can affect the oscillation period strongly (**Fig. S21**).

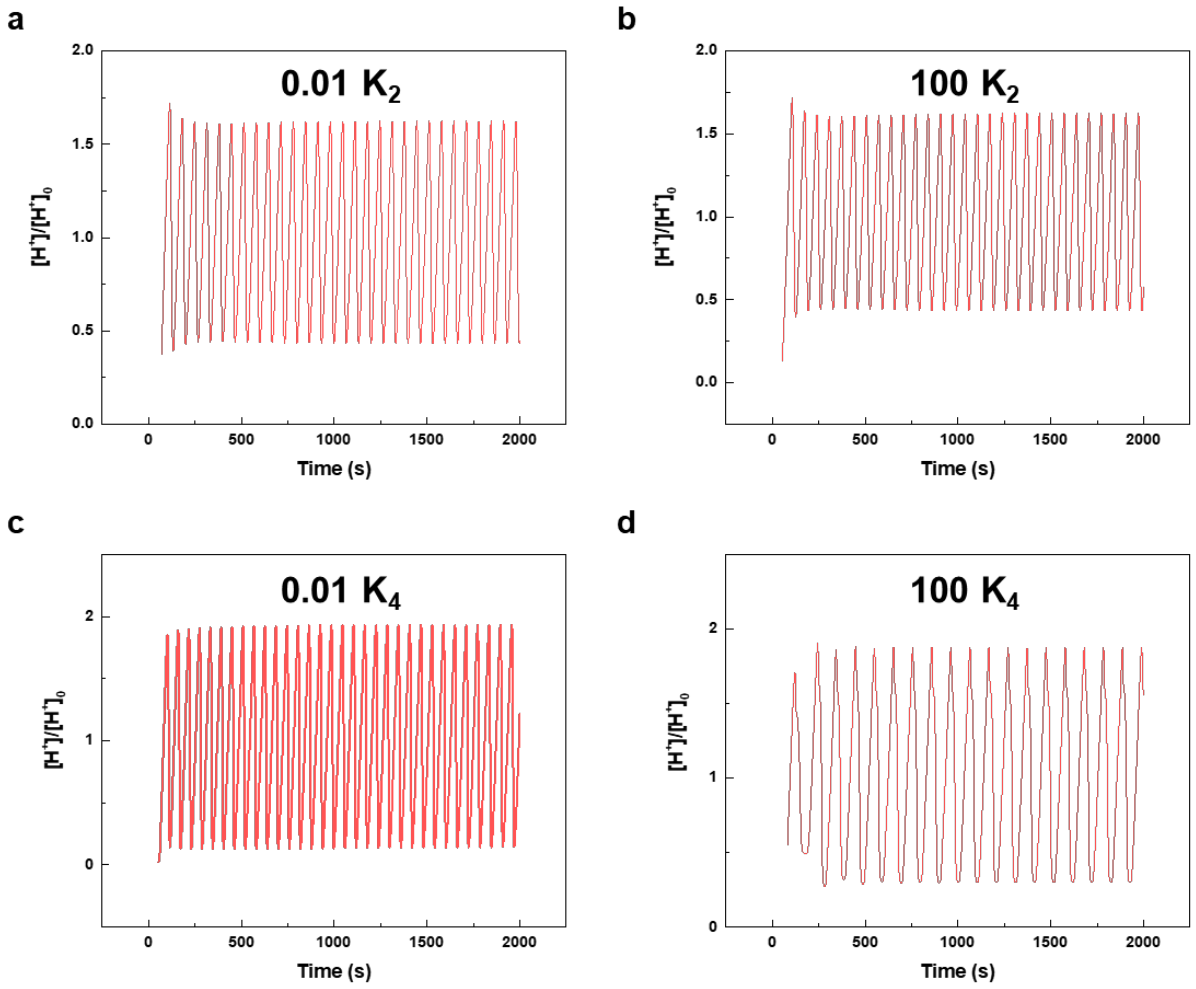

Fig. S20. Proton concentration versus time simulation results. (a) and (b) k_2^0 values are reduced 100 times and increased 100 times, respectively. In both cases, proton concentration oscillations are observed with a period around 70 s without obvious changes. (c) and (d) k_4 values are reduced 100 times (with a period about 60 s) and increased 100 times (with a period about 100 s), respectively. In both cases, proton concentration oscillations are still observed with minor changes in the time periods.

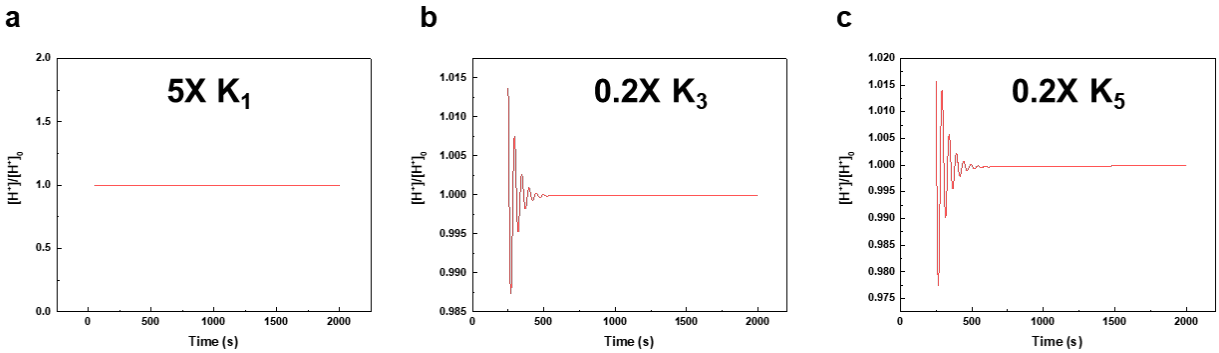

Fig. S21. Proton concentration versus time simulation results. (a) By increasing the k_1 value 5 times larger, the proton concentration oscillation disappears completely. (b) By reducing the k_3 value 5 times smaller, the proton concentration oscillation disappears very soon. (c) By reducing the k_5 value 5 times smaller, the proton concentration oscillation disappears very soon.

Supporting Explanation 2: System Oscillation Study

The stability matrix of the system is established by following standard methods[60], [61] and simplifying the parameter notation as below:

$[-\mathrm{COOH}]: x_1;$ $[\mathrm{H}^+]: x_2;$ $[-\mathrm{COO}^-]: x_3;$ $[-\mathrm{SO_3H}]: x_4;$ $[-\mathrm{SO_3}^-\mathrm{N}^+]: x_5;$
$[-\mathrm{SO_3}^-]: x_6;$ $[-\mathrm{N}^+-]: x_7;$
$Total\ [-\mathrm{SO_3}^-\mathrm{N}^+]: A;$
$Total\ [-\mathrm{COOH}]: B;$

The relationships of these variables can be derived as:

$$\begin{cases} x_7 + x_5 = A \\ x_5 + x_4 + x_6 = A \\ x_1 + x_3 = B \end{cases} \tag{8}$$

$$\begin{cases} \dfrac{dx_2}{dt} = k_1 x_1 - k_3 x_6 x_2 \\ \dfrac{dx_1}{dt} = -k_1 x_1 + k_4 x_4 x_3 \\ \dfrac{dx_6}{dt} = k_2 x_5 - k_3 x_6 x_2 + k_4 x_4 x_3 \\ \dfrac{dx_5}{dt} = -k_2 x_5 + k_5 x_6 x_7 \end{cases} \tag{9}$$

From Eq.(8), x_7 can be derived by x_5; x_3 can be derived by x_1, and x_4 can be derived by x_1 and x_6, and the seven variables (x_1, x_2, x_3, x_4, x_5, x_6, x_7) can be reduced to four variables (x_1, x_2, x_5, x_6,) as

$$\begin{cases} \dfrac{dx_2}{dt} = k_1x_1 - k_3x_6x_2 \\ \dfrac{dx_1}{dt} = -k_1x_1 - k_4Bx_5 - k_4Bx_6 - k_4Ax_1 + k_4x_1x_5 + k_4x_1x_6 + k_4AB \\ \dfrac{dx_6}{dt} = k_2x_5 - k_3x_6x_2 - k_4Bx_5 - k_4Bx_6 - k_4Ax_1 + k_4x_1x_5 + k_4x_1x_6 + k_4AB \\ \dfrac{dx_5}{dt} = -k_2x_5 + k_5Ax_6 - k_5x_5x_6 \end{cases} \quad (10)$$

Small perturbations are added for the system oscillation study:

$$\begin{cases} x_1 = x_{10} + \delta_1 \\ x_2 = x_{20} + \delta_2 \\ x_5 = x_{50} + \delta_5 \\ x_6 = x_{60} + \delta_6 \end{cases} \quad (11)$$

where δ_i are small variations of each corresponding variables and the dynamic equations can be written in the following form (neglecting the constant terms):

$$\begin{bmatrix} \dfrac{dx_2}{dt} \\ \dfrac{dx_1}{dt} \\ \dfrac{dx_6}{dt} \\ \dfrac{dx_5}{dt} \end{bmatrix} = \begin{bmatrix} -k_3x_{60} & k_1 & -k_3x_{20} & 0 \\ 0 & -k_1 - k_4A + k_4x_{50} + k_4x_{60} & -k_4B + k_4x_{10} & -k_4B + k_4x_{10} \\ -k_3x_{60} & -k_4A + k_4x_{50} + k_4x_{60} & -k_4B + k_4x_{10} & k_2 - k_4B + k_4x_{10} \\ 0 & 0 & k_5A - k_5x_{50} & -k_2 - k_5x_{60} \end{bmatrix} \begin{bmatrix} \delta_2 \\ \delta_1 \\ \delta_6 \\ \delta_5 \end{bmatrix} \quad (12)$$

The stability matrix of this system is:

$$\begin{bmatrix} -k_3x_{60} & k_1 & -k_3x_{20} & 0 \\ 0 & -k_1 - k_4A + k_4x_{50} + k_4x_{60} & -k_4B + k_4x_{10} & -k_4B + k_4x_{10} \\ -k_3x_{60} & -k_4A + k_4x_{50} + k_4x_{60} & -k_4B + k_4x_{10} & k_2 - k_4B + k_4x_{10} \\ 0 & 0 & k_5A - k_5x_{50} & -k_2 - k_5x_{60} \end{bmatrix} \quad (13)$$

Here, k_i, A and B are parameters in the simulation, and $x_{10,20,50,60}$ are the solutions of:

$$\begin{cases} \dfrac{dx_2}{dt} = k_1x_1 - k_3x_6x_2 = 0 \\ \dfrac{dx_1}{dt} = -k_1x_1 - k_4Bx_5 - k_4Bx_6 - k_4Ax_1 + k_4x_1x_5 + k_4x_1x_6 + k_4AB = 0 \\ \dfrac{dx_6}{dt} = k_2x_5 - k_3x_6x_2 - k_4Bx_5 - k_4Bx_6 - k_4Ax_1 + k_4x_1x_5 + k_4x_1x_6 + k_4AB = 0 \\ \dfrac{dx_5}{dt} = -k_2x_5 + k_5Ax_6 - k_5x_5x_6 = 0 \end{cases} \quad (14)$$

It is found that the above equation set has no solutions and this means there is no stability matrix, such

that the system is chaotic with hidden attractors[62]. **Figure S22** are the phase portraits for a simulation time of 5,000 s to show the behavior of the system and the projections of those attractors. The parameters used in this exemplified study are those listed in Supporting Explanation 1 (with an oscillation period of 70 s). Since the system is chaotic, the phase portraits will change and cannot be predicted with a different set of parameters.

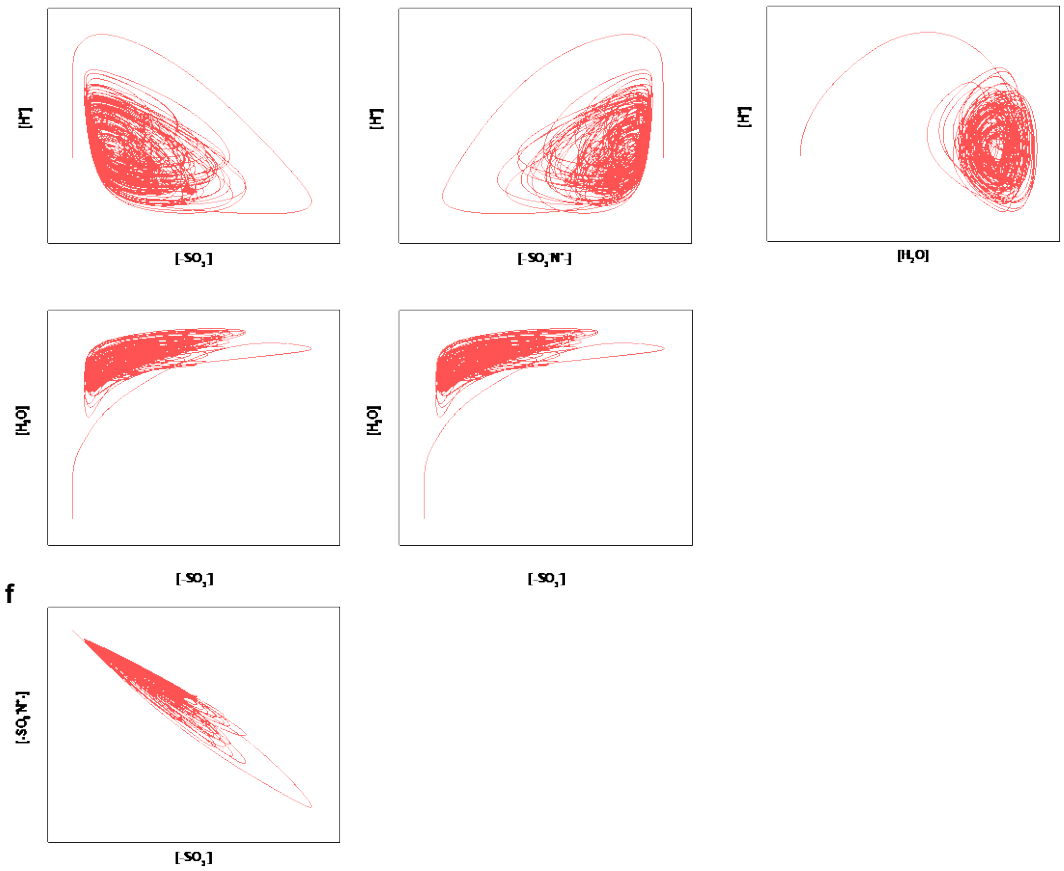

Fig. S22. The phase portraits of the system, showing the oscillating and chaotic behaviors. The above six figures are projections on different concentration coordinate systems in the four-dimensional space. The projection planes are (a) H^+ and $-SO_3^-$; (b) H^+ and $-SO_3^-N^+$; (c) H^+ and H_2O; (d) H_2O and $-SO_3^-$; (e) H_2O and $-SO_3^-N^+$; (f) $-SO_3^-N^+$ and $-SO_3^-$.

Supporting Explanation 3:

Table S2. Analogy to Ca^{2+} oscillation

Ca^{2+} oscillation	This work	Similarity
IP_3	H_2O	Start the oscillation
Ca^{2+}	H^+	Oscillated signal
1st pool	-COOH	In positive feedback(s)
2nd pool	$-SO_3^-$	In negative feedback(s)

IP_3 plays a role similar to H_2O to start the oscillation process; the 1^{st} pool and -COOH groups can execute the positive feedback part of the oscillation procedure, and the 2^{nd} pool and $-SO_3^-$ groups play the role to complete the negative feedback part of the oscillation process.

Reference

[1] G. Liu *et al.*, "An ecological risk assessment of heavy metal pollution of the agricultural ecosystem near a lead-acid battery factory," *Ecol. Indic.*, vol. 47, pp. 210–218, Dec. 2014, doi: 10.1016/j.ecolind.2014.04.040.

[2] X. Tian *et al.*, "Environmental impact and economic assessment of secondary lead production: Comparison of main spent lead-acid battery recycling processes in China," *J. Clean. Prod.*, vol. 144, pp. 142–148, Feb. 2017, doi: 10.1016/J.JCLEPRO.2016.12.171.

[3] D. K. Nandakumar, J. V. Vaghasiya, L. Yang, Y. Zhang, and S. C. Tan, "A solar cell that breathes in moisture for energy generation," *Nano Energy*, p. 104263, Nov. 2019, doi: 10.1016/j.nanoen.2019.104263.

[4] X. Chang *et al.*, "Carbon-based CsPbBr 3 perovskite solar cells: all-ambient processes and high thermal stability," *ACS Appl. Mater. Interfaces*, vol. 8, no. 49, pp. 33649–33655, 2016, doi: 10.1021/acsami.6b11393.

[5] F. Yi, Z. Zhang, Z. Kang, Q. Liao, and Y. Zhang, "Recent Advances in Triboelectric Nanogenerator-Based Health Monitoring," *Adv. Funct. Mater.*, p. 1808849, Mar. 2019, doi: 10.1002/adfm.201808849.

[6] F. Zhao, Y. Liang, H. Cheng, L. Jiang, and L. Qu, "Highly efficient moisture-enabled electricity generation from graphene oxide frameworks," *Energy Environ. Sci.*, vol. 9, pp. 912–916, 2016, doi: 10.1039/c5ee03701h.

[7] T. Xu *et al.*, "Electric Power Generation through the Direct Interaction of Pristine Graphene-Oxide with Water Molecules," *Small*, vol. 14, no. 14, p. 1704473, Apr. 2018, doi: 10.1002/smll.201704473.

[8] Y. Liang *et al.*, "Electric power generation via asymmetric moisturizing of graphene oxide for flexible, printable and portable electronics," *Energy Environ. Sci.*, vol. 11, p. 1730, 2018, doi: 10.1039/c8ee00671g.

[9] H. Cheng *et al.*, "Spontaneous power source in ambient air of a well-directionally reduced graphene oxide bulk," *Energy Environ. Sci*, vol. 11, p. 2839, 2018, doi: 10.1039/c8ee01502c.

[10] J. Liu, Y. Qi, D. Liu, D. Dong, D. Liu, and Z. Li, "Moisture-enabled electricity generation from gradient polyoxometalates-modified sponge-like graphene oxide monolith," *J. Mater. Sci.*, vol. 54, pp. 4831–4841, 2019, doi: 10.1007/s10853-018-3183-6.

[11] Y. Huang *et al.*, "Interface-mediated hygroelectric generator with an output voltage approaching 1.5 volts," *Nat. Commun.*, vol. 9, p. 4166, 2018, doi: 10.1038/s41467-018-06633-z.

[12] Q. Li *et al.*, "Flexible carbon dots composite paper for electricity generation from water vapor absorption," *J. Mater. Chem. A*, vol. 6, pp. 10639–10643, 2018, doi: 10.1039/c8ta02505c.

[13] C. Shao *et al.*, "Wearable fiberform hygroelectric generator," *Nano Energy*, vol. 53, pp. 698–705, Nov. 2018, doi: 10.1016/j.nanoen.2018.09.043.

[14] K. Liu *et al.*, "Induced Potential in Porous Carbon Films through Water Vapor Absorption," *Angew. Chemie*, vol. 128, no. 28, pp. 8135–8139, Jul. 2016, doi: 10.1002/ange.201602708.

[15] T. Xu *et al.*, "An efficient polymer moist-electric generator," *Energy Environ. Sci.*, vol. 12, pp. 972–928, 2019, doi: 10.1039/C9EE00252A.
[16] X. Nie, B. Ji, N. Chen, Y. Liang, Q. Han, and L. Qu, "Gradient doped polymer nanowire for moistelectric nanogenerator," *Nano Energy*, vol. 46, pp. 297–304, Apr. 2018, doi: 10.1016/j.nanoen.2018.02.012.
[17] Z. Luo, C. Liu, and S. Fan, "A moisture induced self-charging device for energy harvesting and storage," *Nano Energy*, vol. 60, pp. 371–376, Mar. 2019, doi: 10.1016/J.NANOEN.2019.03.073.
[18] B. Tulachan *et al.*, "Electricity from the Silk Cocoon Membrane," *Sci. Rep.*, vol. 4, p. 5434, 2014, doi: 10.1038/srep05434.
[19] Z. Zhen, Z. Li, X. Zhao, Y. Zhong, M. Huang, and H. Zhu, "A non-covalent cation-π interaction-based humidity-driven electric nanogenerator prepared with salt decorated wrinkled graphene," *Nano Energy*, vol. 62, pp. 189–196, Aug. 2019, doi: 10.1016/j.nanoen.2019.05.026.
[20] D. Shen, M. Xiao, G. Zou, L. Liu, W. W. Duley, and Y. N. Zhou, "Self-Powered Wearable Electronics Based on Moisture Enabled Electricity Generation," *Adv. Mater.*, vol. 30, no. 18, p. 1705925, May 2018, doi: 10.1002/adma.201705925.
[21] T. Gwang Yun, J. Bae, A. Rothchild, and I.-D. Kim, "Transpiration Driven Electrokinetic Power Generator," *ACS Nano*, vol. 13, no. 11, pp. 12703–12709, 2019, doi: 10.1021/acsnano.9b04375.
[22] M. Li *et al.*, "Biological Nanofibrous Generator for Electricity Harvest from Moist Air Flow," *Adv. Funct. Mater.*, vol. 29, p. 1901798, Jun. 2019, doi: 10.1002/adfm.201901798.
[23] X. Liu *et al.*, "Power generation from ambient humidity using protein nanowires," *Nature*, vol. 578, pp. 550–554, 2020, doi: 10.1038/s41586-020-2010-9.
[24] X. Zhang and L. D. Zhao, "Thermoelectric materials: Energy conversion between heat and electricity," *Journal of Materiomics*, vol. 1, no. 2. Chinese Ceramic Society, pp. 92–105, 01-Jun-2015, doi: 10.1016/j.jmat.2015.01.001.
[25] M. Hamid Elsheikh *et al.*, "A review on thermoelectric renewable energy: Principle parameters that affect their performance," *Renewable and Sustainable Energy Reviews*, vol. 30. Pergamon, pp. 337–355, 01-Feb-2014, doi: 10.1016/j.rser.2013.10.027.
[26] R. Freer and A. V Powell, "Realising the potential of thermoelectric technology: a Roadmap," *J. Mater. Chem. C*, vol. 8, p. 463, 2020, doi: 10.1039/c9tc05710b.
[27] S. Twaha, J. Zhu, Y. Yan, and B. Li, "A comprehensive review of thermoelectric technology: Materials, applications, modelling and performance improvement," *Renewable and Sustainable Energy Reviews*, vol. 65. Elsevier Ltd, pp. 698–726, 01-Nov-2016, doi: 10.1016/j.rser.2016.07.034.
[28] R. Yoshida, T. Sakai, S. Ito, and T. Yamaguchi, "Self-Oscillation of Polymer Chains with Rhythmical Soluble-Insoluble Changes," *J. Am. Chem. Soc.*, vol. 124, no. 27, pp. 8095–8098, Jun. 2002, doi: 10.1021/ja012584q.
[29] T. He *et al.*, "Self-Sustainable Wearable Textile Nano-Energy Nano-System (NENS) for Next-Generation Healthcare Applications," *Adv. Sci.*, vol. 6, p. 1901437, 2019, doi:

10.1002/advs.201901437.
[30] O. C. Namli and M. Taya, “Design of Piezo-SMA Composite for Thermal Energy Harvester Under Fluctuating Temperature,” *J. Appl. Mech.*, vol. 78, no. 3, p. 031001, 2011, doi: 10.1115/1.4002592.
[31] U. Adiyan, T. Larsen, J. José Zárate, L. Guillermo Villanueva, and H. Shea, “Shape memory polymer resonators as highly sensitive uncooled infrared detectors,” *Nat. Commun.*, vol. 10, p. 4518, 2019, doi: 10.1038/s41467-019-12550-6.
[32] M. Kanik *et al.*, “Strain-programmable fiber-based artificial muscle,” *Science (80-.).*, vol. 365, pp. 145–150, 2019.
[33] O. Kuksenok, D. Deb, P. Dayal, and A. C. Balazs, “Modeling Chemoresponsive Polymer Gels,” *Annu. Rev. Chem. Biomol. Eng.*, vol. 5, pp. 35–54, 2014, doi: 10.1146/annurev-chembioeng-060713-035949.
[34] K. Homma, T. Masuda, A. Mizutani Akimoto, K. Nagase, T. Okano, and R. Yoshida, “Stable and Prolonged Autonomous Oscillation in a Self-Oscillating Polymer Brush Prepared on a Porous Glass Substrate,” *Langmuir*, vol. 35, no. 30, pp. 9794–9801, Jul. 2019, doi: 10.1021/acs.langmuir.9b00928.
[35] R. Yoshida and T. Ueki, “Evolution of self-oscillating polymer gels as autonomous polymer systems,” *NPG Asia Mater.*, vol. 6, p. e107, 2014, doi: 10.1038/am.2014.32.
[36] V. V. Yashin and A. C. Balazs, “Pattern formation and shape changes in self-oscillating polymer gels,” *Science (80-.).*, vol. 314, no. 5800, pp. 798–801, Nov. 2006, doi: 10.1126/science.1132412.
[37] H. Zhou, Z. Zheng, Q. Wang, G. Xu, J. Li, and X. Ding, “A modular approach to self-oscillating polymer systems driven by the Belousov-Zhabotinsky reaction,” *RSC Adv.*, vol. 5, p. 13555, 2015, doi: 10.1039/c4ra13852j.
[38] K. Kumar *et al.*, “A chaotic self-oscillating sunlight-driven polymer actuator,” *Nat. Commun.*, vol. 7, no. 1, p. 11975, 2016, doi: 10.1038/ncomms11975.
[39] Y. Soo Kim, R. Tamate, A. Mizutani Akimoto, and R. Yoshida, “Recent developments in self-oscillating polymeric systems as smart materials: from polymers to bulk hydrogels,” *Mater. Horizons*, vol. 4, p. 54, 2017, doi: 10.1039/c6mh00435k.
[40] R. Tamate, A. Mizutani Akimoto, and R. Yoshida, “Recent Advances in Self-Oscillating Polymer Material Systems,” *Chem. Rec.*, vol. 16, pp. 1852–1867, Aug. 2016, doi: 10.1002/tcr.201600009.
[41] T. Arimura and M. Mukai, “A self-oscillating gel actuator driven by ferroin,” *Chem. Commun.*, vol. 50, p. 5863, 2014, doi: 10.1039/c4cc01613k.
[42] Y. Takeoka, M. Watanabe, and R. Yoshida, “Self-Sustaining Peristaltic Motion on the Surface of a Porous Gel,” *J. Am. Chem. Soc.*, vol. 125, no. 44, pp. 13320–13321, Oct. 2003, doi: 10.1021/ja036904c.
[43] J. Sneyd *et al.*, “On the dynamical structure of calcium oscillations,” *Proc. Natl. Acad. Sci. U. S. A.*, vol. 114, no. 7, pp. 1456–1461, 2017, doi: 10.1073/pnas.1614613114.
[44] M. D. Bootman, M. J. Berridge, and H. L. Roderick, “Calcium signalling: More messengers, more channels, more complexity,” *Current Biology*, vol. 12, no. 16. Cell Press, pp. R563–

R565, 20-Aug-2002, doi: 10.1016/S0960-9822(02)01055-2.
[45] Z. Lei and P. Wu, “A supramolecular biomimetic skin combining a wide spectrum of mechanical properties and multiple sensory capabilities,” *Nat. Commun.*, vol. 9, no. 1, p. 1134, Dec. 2018, doi: 10.1038/s41467-018-03456-w.
[46] T. Xu, Q. Han, Z. Cheng, J. Zhang, and L. Qu, “Interactions between Graphene-Based Materials and Water Molecules toward Actuator and Electricity-Generator Applications,” *Small Methods*, vol. 2, no. 10, p. 1800108, Oct. 2018, doi: 10.1002/smtd.201800108.
[47] G. Xue *et al.*, “Water-evaporation-induced electricity with nanostructured carbon materials,” *Nat. Nanotechnol.*, vol. 12, no. 4, pp. 317–321, May 2017, doi: 10.1038/nnano.2016.300.
[48] J. Yin *et al.*, “Waving potential in graphene,” *Nat. Commun.*, vol. 5, no. 1, pp. 1–6, May 2014, doi: 10.1038/ncomms4582.
[49] J. generation from the interaction of a liquid droplet and a liquid membrane Nie, Z. Wang, Z. Ren, S. Li, X. Chen, and Z. L. Wang, “Power generation from the interaction of a liquid droplet and a liquid membrane,” *Nat. Commun.*, vol. 10, p. 2264, 2019, doi: 10.1038/s41467-019-10232-x.
[50] H. Yin Yin Nyein *et al.*, “A Wearable Electrochemical Platform for Noninvasive Simultaneous Monitoring of Ca2+ and pH,” *ACS Nano*, vol. 10, no. 7, pp. 7216–7224, Jul. 2016, doi: 10.1021/acsnano.6b04005.
[51] M. Bariya *et al.*, “Roll-to-Roll Gravure Printed Electrochemical Sensors for Wearable and Medical Devices,” *ACS Nano*, vol. 12, no. 7, pp. 6978–6987, Jun. 2018, doi: 10.1021/acsnano.8b02505.
[52] J. Kang, J. B-H Tok, and Z. Bao, “Self-healing soft electronics,” *Nat. Electron.*, vol. 2, pp. 144–150, 2019, doi: 10.1038/s41928-019-0235-0.
[53] W. L. Jorgensen, D. S. Maxwell, and J. Tirado-Rives, “Development and Testing of the OPLS All-Atom Force Field on Conformational Energetics and Properties of Organic Liquids,” *J. Am. Chem. Soc.*, vol. 118, no. 45, pp. 11225–11236, Nov. 1996, doi: 10.1021/ja9621760.
[54] B. Doherty, X. Zhong, S. Gathiaka, B. Li, and O. Acevedo, “Revisiting OPLS Force Field Parameters for Ionic Liquid Simulations,” *J. Chem. Theory Comput.*, vol. 13, no. 12, pp. 6131–6145, Nov. 2017, doi: 10.1021/acs.jctc.7b00520.
[55] T. Li *et al.*, “Cellulose ionic conductors with high differential thermal voltage for low-grade heat harvesting,” *Nat. Mater.*, vol. 18, no. 6, pp. 608–613, Jun. 2019, doi: 10.1038/s41563-019-0315-6.
[56] X. Qi *et al.*, “Investigation of PF6- and TFSI- anion intercalation into graphitized carbon blacks and its influence on high voltage lithium ion batteries,” *Phys. Chem. Chem. Phys.*, vol. 16, no. 46, pp. 25306–25313, Nov. 2014, doi: 10.1039/c4cp04113e.
[57] M. W. Gaultois, T. D. Sparks, C. K. H. Borg, R. Seshadri, W. D. Bonificio, and D. R. Clarke, “Data-Driven Review of Thermoelectric Materials: Performance and Resource Considerations,” *Chem. Mater.*, vol. 25, no. 15, pp. 2911–2920, May 2013, doi: 10.1021/cm400893e.
[58] M. Z. Kufian, S. R. Majid, and A. K. Arof, “Dielectric and conduction mechanism studies of PVA-orthophosphoric acid polymer electrolyte,” *Ionics (Kiel).*, vol. 13, no. 4, pp. 231–234,

2007, doi: 10.1007/s11581-007-0098-7.
[59] Y. Cao *et al.*, “Self-healing electronic skins for aquatic environments,” *Nat. Electron.*, vol. 2, no. 2, pp. 75–82, Feb. 2019, doi: 10.1038/s41928-019-0206-5.
[60] V. T. Pham, C. Volos, S. Jafari, Z. Wei, and X. Wang, “Constructing a novel no-equilibrium chaotic system,” *Int. J. Bifurc. Chaos*, vol. 24, no. 5, p. 1450073, 2014, doi: 10.1142/S0218127414500734.
[61] V.-T. Pham *et al.*, “Coexistence of hidden chaotic attractors in a novel no-equilibrium system,” *Nonlinear Dyn.*, vol. 87, 2017, doi: 10.1007/s11071-016-3170-x.
[62] S. Panahi, V.-T. Pham, K. Rajagopal, O. Boubaker, and S. Jafari, “A New Four-Dimensional Chaotic System With No Equilibrium Point,” in *Recent Advances in Chaotic Systems and Synchronization*, Elsevier, 2019, pp. 63–76.